NASA

MEMORANDUM

STABILITY CHARACTERISTICS OF TWO MISSILES OF FINENESS RATIOS 12 AND 18 WITH SIX RECTANGULAR FINS OF VERY LOW ASPECT RATIO OVER A MACH NUMBER RANGE OF 1.4 TO 3.2

By Allen B. Henning

Langley Research Center
Langley Field, Va.

NATIONAL AERONAUTICS AND SPACE ADMINISTRATION
WASHINGTON
January 1959

[redacted]
NATIONAL AERONAUTICS AND SPACE ADMINISTRATION

MEMORANDUM 12-2-58L

STABILITY CHARACTERISTICS OF TWO MISSILES OF FINENESS RATIOS 12 AND 18 WITH SIX RECTANGULAR FINS OF VERY LOW ASPECT RATIO OVER A MACH NUMBER RANGE OF 1.4 TO 3.2*

By Allen B. Henning

SUMMARY

Two rocket-propelled missiles have been test flown by the Langley Pilotless Aircraft Research Division in order to study the stability characteristics of a body with six rectangular fins of very low aspect ratio. The fins, which had exposed aspect ratios of approximately 0.04 and 0.02 per fin, were mounted on bodies of fineness ratios of 12 and 18, respectively. Each body had a nose with a fineness ratio of 3.5 and a cylindrical afterbody. The body and the fin chord of the model having a fineness ratio of 12 were extended the length of 6 body diameters to produce the model with a fineness ratio of 18. The missiles were disturbed in flight by pulse rockets in order to obtain the stability data. The tests were performed over a Mach number range of 1.4 to 3.2 and a Reynolds number range of 2×10^6 to 21×10^6.

The results of these tests indicate that these configurations with the long rectangular fins of very low aspect ratio showed little induced roll, with the missile of highest fineness ratio and longest fin chord exhibiting the least amount. Extending the body and fin chord of the shorter missile six body diameters and thereby increasing the fin area approximately 115 percent increased the lift-curve slope based on body cross-sectional area approximately 40 to 55 percent, increased the dynamic stability by a substantial amount, and increased the drag from 14 to 33 percent throughout the comparable Mach number range. The center-of-pressure location of both missiles remained constant over the Mach number range.

*Title, Unclassified.

[redacted]

[redacted]

INTRODUCTION

Wings of medium aspect ratio or stabilizing fins have been used to provide the necessary aerodynamic forces required for maneuvering flight for most of the guided missiles. In order to reduce the frontal packaging size and make a more compact missile, the use of fins of very low aspect ratio has been considered. Wind-tunnel studies have been conducted on wing-body combinations with wings of very low aspect ratio in reference 1, on combinations of bodies and wings of low aspect ratio in reference 2, and on missiles with low-span longitudinal strips placed along the body in reference 3. To investigate the presence and the degree of induced roll on winged configurations of low aspect ratio a study has been conducted by the Langley Pilotless Aircraft Research Division on rocket-propelled free-flight configurations having either highly swept wings, flared skirts, or rectangular wings.

An investigation of the stability characteristics of two configurations, each employing six rectangular fins of very low aspect ratio on a cylindrical afterbody, is reported herein. The two rocket-propelled free-flight missiles had body fineness ratios of 12 and 18, with exposed-fin aspect ratios of 0.04 and 0.02 per fin, respectively.

The two missiles were test flown in a Mach number range of 1.4 to 3.2 and a Reynolds number range of 2×10^6 to 21×10^6 at the Pilotless Aircraft Research Station at Wallops Island, Va.

SYMBOLS

All coefficients are based on the body cross-sectional area and the body diameter.

a_N	normal acceleration, g units
a_T	transverse acceleration, g units
A_F	body cross-sectional or frontal area, 0.267 sq ft
b	total fin span, ft
c	fin chord, ft
C_N	normal-force coefficient
C_Y	side-force coefficient

[redacted]

[redacted]

C_R	resultant-force coefficient
C_X	longitudinal-force coefficient
C_m	pitching-moment coefficient
C_n	yawing-moment coefficient
$C_{N_\alpha}, C_{N_{\Delta\alpha}}$	normal-force-curve slope, $\frac{\partial C_N}{\partial \alpha}$ or $\frac{\partial C_N}{\partial\, \Delta\alpha}$, per deg
$C_{Y_\beta}, C_{Y_{\Delta\beta}}$	side-force-curve slope, $\frac{\partial C_Y}{\partial \beta}$ or $\frac{\partial C_Y}{\partial\, \Delta\beta}$, per deg
C_{m_q}	pitch-damping derivative, $\frac{\partial C_m}{\partial\, \frac{\dot{\theta} d}{2V}}$
C_{m_α}	static stability derivative, $\frac{\partial C_m}{\partial \alpha}$
$C_{D_{min}}$	minimum drag coefficient
d	body diameter, 0.583 ft
g	acceleration due to gravity, ft/sec^2
I	moment of inertia about Y- or Z-axis, $slug\text{-}ft^2$
I_X	moment of inertia about X-axis, $slug\text{-}ft^2$
l	body length, ft
M	Mach number
m	mass, slugs
p	rolling velocity, radians/sec
P_{av}	average period of oscillation, sec
q	dynamic pressure, lb/sq ft
r	nose-coordinate radius, in.

[redacted]

R	Reynolds number per foot
t	time, sec
V	velocity, ft/sec
x	distance along body measured from nose, in. or ft
X,Y,Z	body coordinate axis
α	angle of attack, deg
β	angle of sideslip, deg
$\dot{\alpha}$	time rate of change of angle of attack, radians/sec
$\dot{\beta}$	time rate of change of angle of sideslip, radians/sec
$\Delta\alpha$	angle of attack from integration of $\dot{\alpha}$
$\Delta\beta$	angle of sideslip from integration of $\dot{\beta}$
$\dot{\theta}$	pitching velocity, radians/sec
$\dot{\psi}$	yawing velocity, radians/sec
$\dot{\phi}$	rolling velocity, radians/sec
$\ddot{\theta}$	pitching acceleration, radians/sec^2
$\ddot{\psi}$	yawing acceleration, radians/sec^2
ω_o	basic oscillation frequency, radians/sec
λ_o	nonrolling damping constant, 1/sec
$\Delta\lambda$	damping constant due to roll, 1/sec
$\Delta\omega$	component of total pitch frequency resulting directly from roll, radians/sec

Subscript:

c.g.	center of gravity

A dot over a symbol indicates the first derivative with respect to time. Two dots indicate the second derivative.

[redacted]

MODELS

Sketches of the two test missiles showing configuration characteristics and dimensions are presented in figure 1, and photographs of these missiles are shown in figure 2. Also presented in figure 1 are the geometric and mass characteristics for both missiles. The coordinates for the nose section are presented in table I.

The two missiles (referred to herein as model 1 and model 2) were constructed of aluminum alloy, and each had a nose with a fineness ratio of 3.5 and a straight cylindrical afterbody. Six rectangular, thin, aluminum-alloy fins of very low aspect ratio were welded to the cylindrical afterbody. Model 1 had a body length of 12 diameters, a fin chord of 5.14 body diameters, and a total fin span of 1.44 body diameters. Model 2 was similar, except that the body and fin chord lengths were increased 6 diameters to a fineness ratio of 18 and a fin chord of 11.14 body diameters.

The models were disturbed in flight by six pulse rockets that were placed around the body midway between each adjacent pair of fins and positioned to fire in such a direction as to place their lines of thrust through the center line of the model. The longitudinal location of the pulse rockets was near the rear of model 1 and approximately 5/6 the length of the body from the nose of model 2.

A scale model of model 1, shown in figure 3, was flown in conjunction with this investigation in order to obtain drag data for the preliminary calculations. This scale model was tested by the helium-gun technique described in detail in reference 4.

INSTRUMENTATION AND TESTS

The two models used in this investigation had the same instrumentation. Seven instruments, of which three were accelerometers, three were rate gyros, and one was a pressure cell, measured the normal acceleration, lateral acceleration, longitudinal acceleration, rate of pitch, rate of yaw, rate of roll, and total pressure. The flight data measured by the instruments were relayed from the model to the ground station by the standard NACA telemetering system.

Each model was propelled to flight-test velocity by a Nike booster rocket motor. A photograph of the model-booster combination mounted on the launcher prior to firing is presented in figure 4. After burnout of the booster, the model and the booster separated from each other because of the difference in the drag-to-weight ratios. Velocity and flight-path

data were obtained from CW Doppler radar and SCR 584 tracking radar, respectively. The maximum Mach number obtained by models 1 and 2 was 3.34 and 3.03, respectively. Atmospheric data were obtained from a rawinsonde sent aloft with a balloon immediately after each test flight. The Reynolds numbers and dynamic pressures obtained throughout these test flights are presented in figure 5.

The six pulse rockets were programmed to fire in a timed sequence after the model-booster separation. The first two were fired in succession in the vertical plane the second two in a plane inclined 60° to the right of vertical, and the third two in a plane inclined 60° to the left of vertical when referenced from the rear of the model. The resulting programming gave six disturbances from the pulse rockets and one disturbance from the model-booster separation, or seven disturbances or pulses throughout the test Mach number range. Hereafter, these pulses are referred to as separation pulse, first pulse, second pulse, and so forth.

ACCURACY

The systematic errors of the measured quantities caused by the instrument inaccuracies are given in the following table in coefficient form for the forces involved and in radians per second for the rate measurements. The errors are given as incremental errors, and the tabulated coefficients are based on the body cross-sectional area.

Quantity	Model 1		Model 2	
	M = 2.0	M = 3.0	M = 2.0	M = 3.0
C_N	±0.144	±0.026	±0.106	±0.029
C_Y	±.144	±.026	±.106	±.029
C_X	±.096	±.018	±.053	±.015
$\dot{\theta}$	±.4	±.4	±.4	±.4
$\dot{\psi}$	±.4	±.4	±.4	±.4
$\dot{\phi}$	±1.2	±1.2	±1.2	±1.2

The random errors are much smaller than these tabulated systematic errors and may be determined by the scatter of the data. In the calculation of $C_{N_{\Delta\alpha}}$, $C_{Y_{\Delta\beta}}$, $\frac{dC_m}{dC_N}$, and $\frac{dC_n}{dC_Y}$ the systematic, random, and other errors

introduced during the integration and differentiation processes are lessened and perhaps cancelled out when the slope is determined. The errors in Mach number and dynamic pressure are on the order of ±1 percent.

PRESENTATION OF DATA AND METHOD OF ANALYSIS

The body axes coordinate system is used in analyzing the data obtained from the flight tests of the two models. This axes system is shown in figure 6. Also included in figure 6 is the sign convention showing the positive directions of the various quantities used herein.

The time histories of models 1 and 2 are shown in figures 7 and 8 for each pulse-rocket and booster-separation disturbance. The variation with time of the normal- and side-force coefficients; the pitch, yaw, and roll rate; and the Mach number, along with a cross plot of the normal- and the side-force coefficients are presented in these figures. The data plotted herein were continuously measured and recorded throughout the flight and read at intervals of 0.01 second, but in order to permit easier reading of the figures only the faired values of the measured quantities are shown.

In analyzing the data obtained from the instruments of the flight models, the following applications were used: (1) The normal-force- and side-force-curve slopes were determined from the pitch and yaw rates, (2) The pitching-moment and the yawing-moment coefficients were calculated from the pitch and yaw rates, and (3) The static and dynamic stability derivatives were computed from the cross plots of the normal-force and side-force coefficients (ref. 5).

The rates of pitch and yaw, along with the normal and transverse accelerations, were used to calculate the time rate of change of angle of attack and the time rate of change of angle of sideslip. These relationships were determined thusly;

$$\dot{\alpha} = \dot{\theta} - \frac{a_{N_{c.g.}} g}{V} - \dot{\phi}\beta$$

and

$$\dot{\beta} = -\dot{\psi} + \frac{a_{T_{c.g.}} g}{V} + \dot{\phi}\alpha$$

where α and β are approximated by $\frac{C_N}{C_{N_\alpha}}$ and $\frac{C_Y}{C_{Y_\beta}}$, respectively, by using theoretical calculations for C_{N_α} and C_{Y_β}. The $\dot{\alpha}$ and $\dot{\beta}$ curves were plotted against time and then integrated about arbitrary axes which, in this case, were their zero axes. Since these arbitrary axes are not necessarily the correct axes about which to integrate, an integration constant correction had to be made to give the integration results, $\Delta\alpha$ and $\Delta\beta$ curves, their correct slopes. It is assumed in the case of a symmetrical missile that at the time the normal-force coefficient C_N is equal to zero the angle of attack α is also equal to zero. The $\Delta\alpha$ curve is then corrected for this assumption by integrating $\dot{\alpha}$ about the corrected axis. This assumption holds for the side-force coefficient C_Y and the angle of sideslip β, in that $C_Y = 0$ when $\beta = 0$, and then the $\Delta\beta$ curve is corrected by integrating $\dot{\beta}$ about the corrected axis. The resulting $\Delta\alpha$ and $\Delta\beta$ curves are plotted, respectively, with C_N and C_Y, and their slopes are the normal-force-curve slope $C_{N_{\Delta\alpha}}$ and the side-force-curve slope $C_{Y_{\Delta\beta}}$. An example of a typical variation of C_N with $\Delta\alpha$ and C_Y with $\Delta\beta$ for model 1 is shown in figure 9. Even though the integration does not give the exact numerical values of α and β, it provides a suitable value for the determination of the normal-force-curve slope $C_{N_{\Delta\alpha}}$ and the side-force-curve slope $C_{Y_{\Delta\beta}}$ $\left(\text{referred to as } C_{N_\alpha} \text{ and } C_{Y_\beta}, \text{ respectively}\right)$.

The pitching-moment coefficient C_m and the yawing-moment coefficient C_n were calculated by using the following relationships:

$$C_m = \left(\frac{I}{qA_F d}\right)(\ddot{\theta} - \dot{\phi}\dot{\psi})$$

and

$$C_n = \left(\frac{I}{qA_F d}\right)(\ddot{\psi} + \dot{\phi}\dot{\theta})$$

where the pitch acceleration $\ddot{\theta}$ and the yaw acceleration $\ddot{\psi}$ were obtained by differentiating the $\dot{\theta}$ and $\dot{\psi}$ curves with respect to time. The resultant quantities of C_m and C_n were then plotted against C_N and C_Y. The average slopes of these curves were measured to obtain a

value of $\frac{dC_m}{dC_N}$ and $\frac{dC_n}{dC_Y}$. The center of pressure or aerodynamic-center location in percent of body length is calculated by using the equation:

$$c.p. = \left[\frac{x_{c.g.}}{l} - \left(\frac{dC_m}{dC_N}\right)\left(\frac{d}{l}\right)\right]100$$

or

$$c.p. = \left[\frac{x_{c.g.}}{l} - \left(\frac{dC_n}{dC_Y}\right)\left(\frac{d}{l}\right)\right]100$$

The method employed to extract the stability derivatives from the oscillations of these models is described in detail in reference 5. In this method it is assumed that the models are symmetrical, that they have a constant trim point, and that the rate of roll is constant. The cross plot of C_N and C_Y is utilized to determine the stability roots which are the basic oscillation frequency ω_o, the nonrolling damping constant λ_o, the damping constant due to roll $\Delta\lambda$, and the component of the total pitch frequency resulting directly from roll $\Delta\omega$. In all cases $\Delta\omega$ was determined from the average roll rate for each pulse by using equation 16 of reference 5 where $\Delta\omega = p\left(1 - \frac{I_X}{2I}\right)$. The stability roots were calculated for both model 1 and model 2 and are presented in table II. The method presented in reference 6 was also incorporated in the data reduction, and these results are also shown. By using the following equations, C_{m_q} and C_{m_α} can be determined:

$$C_{m_q} = \left[\left(\frac{2I}{qA_Fd}\right)(\lambda_o) + \frac{57.3C_{N_\alpha}I}{mVd}\right]\left(\frac{2V}{d}\right)$$

and

$$C_{m_\alpha} = -\left(\frac{I}{qA_Fd}\right)\left[\omega_o^2 + \lambda_o^2 - \Delta\lambda^2 - \frac{\left(\frac{I_X}{2I}\right)^2}{\left(1 - \frac{I_X}{2I}\right)^2}(\Delta\omega^2)\right] - \frac{57.3C_{N_\alpha}C_{m_q}qA_Fd}{2mV^2}$$

Values measured for C_{N_α} by the previous method may be compared with values determined by using the following equation which utilizes the stability roots computed from the cross plots of C_N and C_Y

$$C_{N_\alpha} = -\left(\frac{1}{\frac{dC_m}{dC_N}}\right)\left[\frac{I}{qA_F d(57.3)}\right]\left[\omega_o^2 + \lambda_o^2 - \Delta\lambda^2 + \Delta\omega^2 \frac{\frac{I_X}{I}\left(1 - \frac{I_X}{4I}\right)}{\left(1 - \frac{I_X}{2I}\right)^2}\right]$$

In order to reduce the data by the method of reference 5, a constant trim point had to be selected for each pulse, and from this point the resultant coefficient C_R was determined. The trim points for each pulse of model 1 were located at some small value of $+C_N$ and $+C_Y$ to indicate that the model had a trim level at some small resultant angle of attack. Similarly, for model 2, a constant trim point was selected for each pulse, but in this case the trim point was at a higher $+C_N$ and $+C_Y$ position and indicated that the model trimmed at a higher resultant angle of attack. This trim position remained in the same cross-plot quadrant throughout the flight, with the resultant angle-of-attack magnitude decreasing with decreasing Mach number, especially in the fifth and sixth pulses.

The data from the separation pulse and the first pulse of model 2 could not be completely determined. Observation of the telemeter record indicates that the booster rocket motor interfered with the model flight during separation up to the flight time of 3.9 seconds. The remaining portion of this separation disturbance was not long enough for good analysis, and because of the early firing of the second pulse rocket, the disturbance from the first pulse rocket was too short for any analysis; therefore, the stability roots could not be determined from these two model disturbances.

A comparison of the cross plots of figures 7 and 8 with similar cross plots of reference 5 shows that at no time during the test flight did the models approach a resonant condition, where $\frac{\Delta\omega}{\omega_o} = 1.0$. Throughout the flights of both models the roll rates were small, and the greatest value of $\frac{\Delta\omega}{\omega_o}$ was of the order of 0.2.

The results of the data analysis are presented in figures 10 to 16.

[redacted]

RESULTS AND DISCUSSION

Induced Roll

When a symmetrical missile is at some angle of attack the asymmetrical flow about the missile can impart an induced roll to the configuration. In order to establish the amount of roll induced into the configuration, the rates of roll of the two test models were measured and the time histories of the roll rates are included in figures 7 and 8. In the design of these models the pulse rockets were placed to fire normal to and through the center line of each model, but because of construction tolerances the pulse rockets could be slightly misalined to produce a roll at the time of firing; therefore, at the beginning of each pulse the model had some roll, either positive or negative. Any increase in the roll rate after the pulse rocket had finished firing could be considered as being induced by configuration or flow asymmetries. When observing the roll-rate time histories of figures 7 and 8 it is noted that there is no constant roll buildup in any one direction, which signifies that roll induced by the configuration asymmetries is small; therefore, it is assumed that the majority of the roll-rate increase with time, positive or negative, would be induced by the flow asymmetries. A decrease of the roll rate probably would be caused by the roll damping of the configuration, but an increase probably would signify aerodynamically induced roll. In all cases the roll rate is low and any change due to induced roll, that is, increasing roll magnitude either positive or negative, is small. In general, these configurations with the long rectangular fins of very low aspect ratio showed little induced roll, and the model of highest fineness ratio and longest fin chord exhibited the least amount.

Normal- and Side-Force-Curve Slopes

The variation with Mach number of the normal-force-curve slope and the side-force-curve slope for models 1 and 2 is presented in figure 10(a) and 10(b), respectively. Also included in figure 10 are some referenced test data for a model similar to model 1 and for body-alone tests for tangent-ogive-nose-cylinder afterbody models with overall fineness ratios of 12 and 18. Theoretical calculations from reference 7 for similar configurations are also presented as a check on the validity of the test data.

The $C_{N_{\Delta\alpha}}$ and $C_{Y_{\Delta\beta}}$ points for each model show no appreciable difference, other than scatter, between the overall $C_{N_{\Delta\alpha}}$ and $C_{Y_{\Delta\beta}}$ levels and thus indicate that the symmetrical-model assumption is valid; therefore, under this assumption, $C_{N_{\Delta\alpha}} = C_{Y_{\Delta\beta}}$ and one line is shown faired through

[redacted]

the scattered $C_{N_{\Delta\alpha}}$ and $C_{Y_{\Delta\beta}}$ points to represent the variation of the normal-force-curve slope with Mach number. The faired line of model 1 for C_{N_α} compares favorably with the theoretical calculations, but that of model 2 has an unfavorable comparison in that the theoretical curve is 11 to 16 percent higher than the faired values of the calculated points. These data for model 2 could be expected to be of a higher value because cross plots of model 2 show that the model trimmed at high values of C_N and C_Y and, therefore, indicate the trim to be at some angle of attack other than zero, which according to the normal-force-curve characteristics of this type of configuration would increase the C_{N_α} to the value corresponding to the trim angle of attack.

Another means of calculating C_{N_α} explained in "Presentation of Data and Method of Analysis" utilizes the stability roots presented in table II. The results of this calculation are also tabulated in table II. By comparing these values with those of figure 10 it can be noted that the calculated values for model 1 are slightly lower but compare favorably with the plotted values, but for model 2 they vary considerably. These C_{N_α} values are dependent on the $\frac{dC_m}{dC_N}$ values, that are presented in the "Center of Pressure" section, and any appreciable change in $\frac{dC_m}{dC_N}$ would change C_{N_α}. The C_{N_α} values of figure 10 are the values referred to herein unless otherwise noted.

A C_{N_α} test point from reference 8 for a model 14 body diameters long having 4 fins 5 diameters long and a total span of 1.5 diameters is used for comparison with model 1. This point is slightly lower in magnitude but presents a good comparison when it is considered that only 4 fins are involved. A visual comparison between data for similar models of references 8 and 9 with 4 and 6 fins was made, and it was noted that the model with 6 fins had an increase in C_{N_α} of about 8 percent over the model with 4 fins; therefore, with a similar increase to the referenced point, the comparison shown in figure 10 would be even better.

The body-alone data of references 10 and 11 are presented herein as an aid in calculating the theoretical values of C_{N_α} for both models and to show the increment of normal force contributed by the fins and the fin-body interference. By comparing the body-alone data with the test data it can be seen that a considerable increase in C_{N_α} is

realized by adding these fins of very low aspect ratio to each of the bodies having fineness ratios of 12 and 18.

Finally, in comparing models 1 and 2 with each other it is shown that by increasing the length of the afterbody and fins of model 1 6 body diameters and thereby increasing the actual fin area approximately 115 percent increases the C_{N_α}, based on body cross-sectional area, 40 to 55 percent over the comparable Mach number range.

Period and Damping of the Longitudinal Oscillation

The period of the longitudinal oscillation of models 1 and 2 throughout the test Mach number range is presented in figure 11. Each symboled point shown in the figure is the average period for each pulse and was obtained from the time-history oscillation of the resultant coefficient calculated from the cross plot of C_N and C_Y by the method of reference 5. The period curve of model 2 increases sharply at the low test Mach numbers, but it is not known whether model 1 shows this trend or not as no data were available at these Mach numbers. At comparable Mach numbers, the period of model 2 is approximately one-half that of model 1.

The exponential damping constant λ_o for models 1 and 2 is presented in figure 12. The symboled points represent the data that were derived from the envelope of the resultant coefficient as explained in reference 5. Along with the data of model 1 are a few check points determined, whenever possible, by the method employed in reference 6. In comparing these two methods, a good agreement is in evidence for the few points checked. The damping data for model 2 above a Mach number of 2.6 were unobtainable because of the difficulties explained previously. The damping factor increases with an increase in Mach number, and model 2 shows a considerable increase over that of model 1.

The dynamic damping derivative C_{m_q} is a direct function of the damping factor, and its variation with Mach number is shown in figure 13. As can be seen by both figure 12 and figure 13 the damping of model 1 is low, but by adding 6 diameters of length to the body and fin chord and thereby approximately doubling the area of the fins, the damping is considerably increased throughout the test Mach number range.

Static Stability

The static stability derivative C_{m_α} is plotted against Mach number and presented in figure 14 for both models. These curves were derived by the equation shown in "Presentation of Data and Method of

Analysis" by using the stability roots given in table II. These plots show that the static stability of model 2 is much higher than that of model 1. The largest quantities in the calculation of C_{m_α} are the oscillation frequency and the exponential damping factor, and, since for model 2 these quantities are quite high, the derived values of the static stability can become quite large also and thereby show a large increase in static stability for this model over that of model 1. This large increase can possibly be attributed to the increase in fin area, most of which is behind the center of gravity.

Center of Pressure

The C_m and C_n values were determined from calculations made by the method given in "Presentation of Data and Method of Analysis" and plotted against C_N and C_Y, respectively. The resulting slopes $\frac{dC_m}{dC_N}$ and $\frac{dC_n}{dC_Y}$ represent the static margin of the missile or the distance from the center of pressure to the center of gravity, and these slopes are plotted against Mach number in figure 15(a) for models 1 and 2. Each symboled point represents either $\frac{dC_m}{dC_N}$ or $\frac{dC_n}{dC_Y}$ over the time of one pulse, and the dashed line represents the faired average of these points over the Mach number range. These average values were used to calculate, by the method discussed previously, the C_{N_α} values that are given in table II. By utilizing the C_{m_α} values from figure 14 and the C_{N_α} values from figure 10 a comparison of $\frac{C_{m_\alpha}}{C_{N_\alpha}}$ is made with the data in figure 15(a). The $\frac{C_{m_\alpha}}{C_{N_\alpha}}$ of model 1 compares favorably with the $\frac{dC_m}{dC_N}$ and $\frac{dC_n}{dC_Y}$ values, but for model 2 the comparison is not as good.

The results of figure 15(a) are transformed into a ratio of center-of-pressure location to body length and presented in figure 15(b). Included in this figure is the center of pressure calculated from the theory of reference 7. The data of model 1 compare very well with the theory, but the data of model 2 show a center-of-pressure location somewhat forward of the predicted theory. The center of pressure of

models 1 and 2 calculated from $\frac{dC_m}{dC_N}$ and $\frac{dC_n}{dC_Y}$ is fairly constant throughout the test Mach number range.

Minimum Drag

The variation of the minimum-drag coefficient with Mach number is presented in figure 16 for both models. The test points shown were determined from the polars of the longitudinal-force coefficient C_X and the resultant-force coefficient C_R, where $C_R = \sqrt{C_N^2 + C_Y^2}$. Since these models were assumed to be symmetrical, the minimum point was taken to be the point at which the resultant-force coefficient equalled zero. In some cases, particularly in the case of model 2, the polar curve had to be extrapolated to $C_R = 0$ because of the large minimum value of C_R; consequently, the accuracy of the drag curve for model 2, even though the polars were fairly flat, would not be as good as that of model 1. Included in the figure is the drag obtained from the helium-gun test of the scale model of model 1. A comparison of the drag of models 1 and 2 shows that model 2 had approximately 14 to 33 percent more drag than model 1 between the Mach numbers of 2 and 3. This increase in drag was mainly skin-friction drag due to the increased wetted area caused by elongating the body and increasing the fin area.

CONCLUSIONS

Two rocket-propelled missiles have been test flown in order to study the stability characteristics of a body with six rectangular fins of very low aspect ratio. The fins had aspect ratios of 0.04 and 0.02 and were mounted on bodies which had fineness ratios of 12 and 18, respectively. Each of the bodies had a nose with a fineness ratio of 3.5 and a cylindrical afterbody. The tests covered the Mach number range of 1.4 to 3.2.

From these tests the following conclusions have been made:

1. These configurations with the long rectangular fins of very low aspect ratio showed little induced roll, and the model of highest fineness ratio and longest fin chord exhibited the least amount.

2. Increasing the length of the afterbody and fins of the shorter model 6 body diameters and thereby increasing the actual fin area approximately 115 percent increases the C_{N_α}, based on body cross-sectional area, 40 to 55 percent over the comparable Mach number range.

[redacted]

3. Lengthening the body and fins and thereby increasing the fin area increases the damping and, consequently, the dynamic stability by a substantial amount.

4. The center of pressure of each model is fairly constant throughout the test Mach number range.

5. Increasing the wetted area by elongating the body and fins increased the drag from 14 to 33 percent between Mach numbers of 2 and 3.

Langley Research Center,
National Aeronautics and Space Administration,
Langley Field, Va., October 1, 1958.

[redacted]

REFERENCES

1. Jorgensen, Leland H., and Katzen, Elliott D.: Wing-Body Combinations With Wings of Very Low Aspect Ratio at Supersonic Speeds. NACA RM A56G16, 1956.

2. Robinson, Ross B.: Aerodynamic Characteristics of Missile Configurations With Wings of Low Aspect Ratio for Various Combinations of Forebodies, Afterbodies, and Nose Shapes for Combined Angles of Attack and Sideslip at a Mach Number of 2.01. NACA RM L57D19, 1957.

3. Spearman, M. Leroy, and Robinson, Ross B.: Aerodynamic Characteristics of a Cruciform-Wing Missile With Canard Control Surfaces and of Some Very Small Span Wing-Body Missiles at a Mach Number of 1.41. NACA RM L54B11, 1954.

4. Hall, James Rudyard: Comparison of Free-Flight Measurements of the Zero-Lift Drag Rise of Six Airplane Configurations and Their Equivalent Bodies of Revolution at Transonic Speeds. NACA RM L53J21a, 1954.

5. Nelson, Robert L.: The Motions of Rolling Symmetrical Missiles Referred to a Body-Axis System. NACA TN 3737, 1956.

6. Baber, Hal T., Jr., and Moul, Martin T.: Longitudinal Stability and Control Characteristics as Determined by the Rocket-Model Technique for an Inline, Cruciform, Canard Missile Configuration With a Low-Aspect-Ratio Wing Having Trailing-Edge Flap Controls for a Mach Number Range of 0.7 to 1.8. NACA RM L54B12, 1955.

7. Luther, M. L.: The Supersonic Lift and Centers of Pressure of Rectangular Fin Assemblies in Combination With a Long, Cylindrical Body. NAVORD Rep. 1249 (NOTS 312), U. S. Naval Ord. Test Station, Inyokern (China Lake, Calif.), Aug. 23, 1950.

8. Jaeger, B. F., deLancey, L. M., and Schroedter, G. M.: Aerodynamic Characteristics at Mach Number 2.87 of 14- and 18-Caliber Fin-Stabilized Rocket Models With Varying Fin Parameters. NAVORD Rep. 1331 (NOTS 411), U. S. Naval Ord. Test Station, Inyokern (China Lake, Calif.), July 24, 1951.

9. Jaeger, B. F., and deLancey, L. M.: The Aerodynamic Characteristics at Mach Number 1.87 of 14- and 18-Caliber Fin-Stabilized Rocket Models With Varying Fin Parameters. NAVORD Rep. 1918 (NOTS 447), U. S. Naval Ord. Test Station, Inyokern (China Lake, Calif.), Oct. 10, 1951.

[redacted]

10. Darling, J. A., and DeMeritte, F. J.: Aeroballistics Research Investigation of NOTS Rockets. NAVORD Rep. 1506 (Aeroballistic Res. Rep. 3), U. S. Naval Ord. Lab. (White Oak, Md.), Dec. 6, 1950.

11. Krieger, R. H., and Hughes, J. M.: Wind Tunnel Tests on British Finned Models With Varying Body and Fin Parameters. Memo. Rep. No. 768, Ballistic Res. Labs., Aberdeen Proving Ground, Mar. 1954.

[redacted]

TABLE I.- NOSE COORDINATES

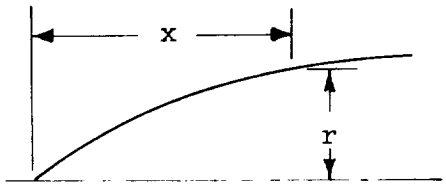

x	r
0	0.168
.060	.182
.122	.210
.245	.224
.480	.294
.735	.350
1.225	.462
2.000	.639
2.450	.735
4.800	1.245
7.350	1.721
8.000	1.849
9.800	2.155
12.250	2.505
13.125	2.608
14.375	2.747
14.700	2.785
17.150	3.010
19.600	3.220
22.050	3.385
24.500	3.500
25.000	3.500

TABLE II.- VALUES OF STABILITY ROOTS AND C_{N_α}

[Determined by method of reference 5]

Pulse	ω_o	λ_o	$\Delta\omega$	$\Delta\lambda$	M	C_{N_α}
Model 1						
Separation	18.59* ------	-2.39* -------	------	------	3.21	-----
First	14.88	-1.88* -2.050	-3.22	0.182	2.92	0.101
Second	14.16	-1.346	-1.84	-0.385	2.72	0.103
Third	13.13	-1.182	-2.97	-0.112	2.57	0.096
Fourth	11.11	-1.12* -1.176	-1.29	0.043	2.40	0.084
Fifth	10.42	-0.910* -.907	-2.08	0.098	2.17	0.105
Sixth	9.03	-0.716	-1.27	0.087	1.96	0.119
Model 2						
Separation	33.9	-------	------	------	2.86	-----
First	------	-------	------	------	2.67	-----
Second	28.25	-6.075	1.166	1.195	2.54	0.260
Third	22.10	-3.620	-2.540	------	2.28	0.225
Fourth	19.38	-2.887	-4.310	0.233	2.00	0.280
Fifth	10.87	-1.570	0.600	0	1.61	0.206
Sixth	6.53	-0.804	1.012	0	1.41	0.138

*Values obtained by using method of reference 6.

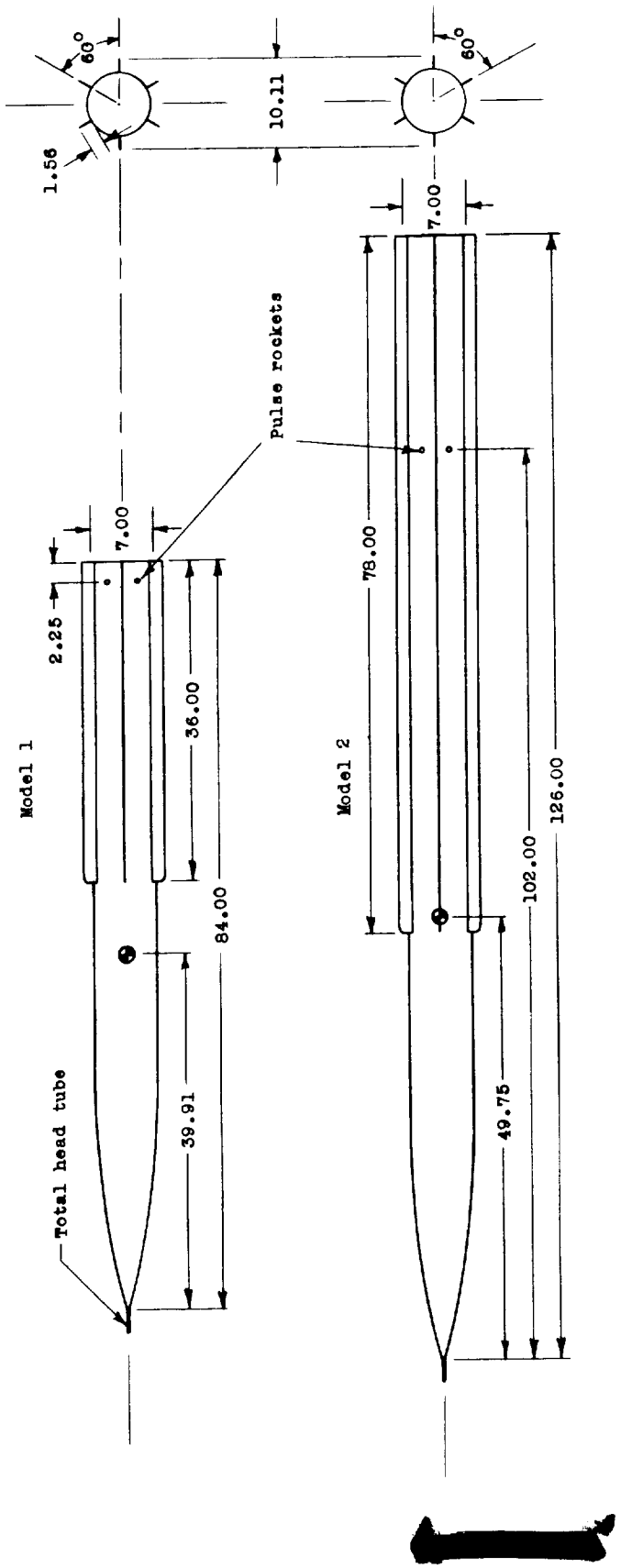

GEOMETRIC AND MASS CHARACTERISTICS

	Model 1	Model 2
Exposed fin area, in one plane, sq ft	0.78	1.68
Body cross-sectional area, reference area, ft^2	0.267	0.267
Aspect ratio, per fin	0.043	0.020
l/d	12.00	18.00
c/d	5.14	11.14
b/d	1.44	1.44
Weight, lb_2	103.90	106.50
I, $slug\text{-}ft^2$	14.27	21.81
I_x, $slug\text{-}ft^2$	0.138	0.148

Figure 1.- Dimensional drawing and mass characteristics of the low-aspect-ratio test missiles. All linear dimensions are in inches.

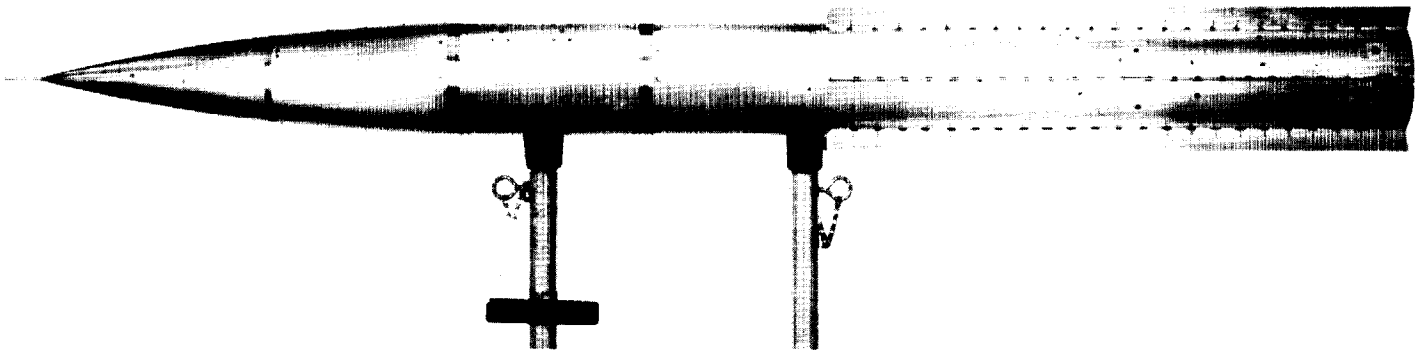

Model 1

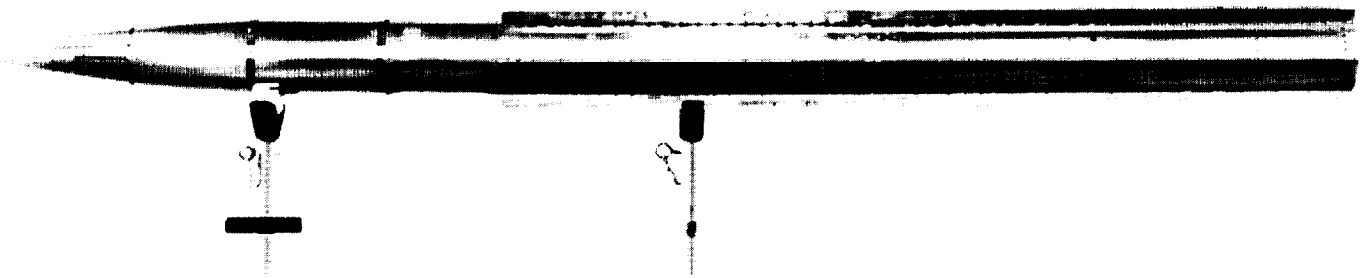

Model 2

Figure 2.- Photographs of flight missiles. L-58-2569

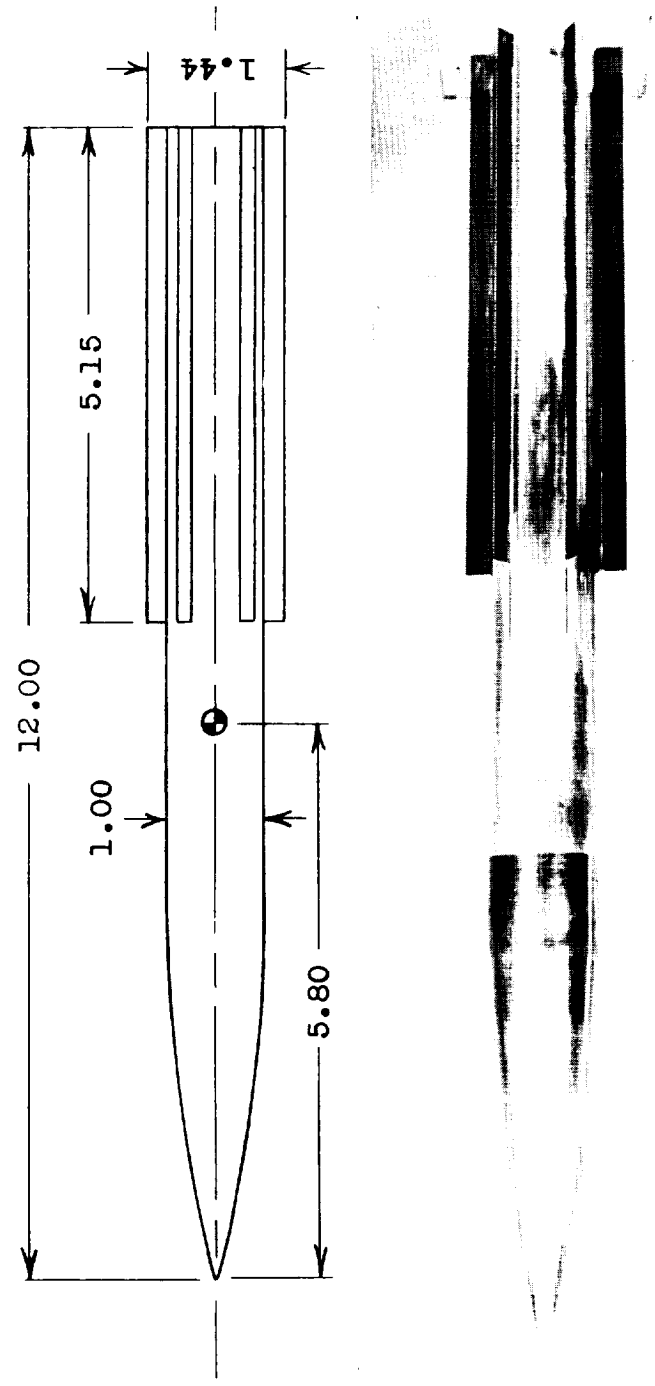

L-90872.1

Figure 3.- Drawing and photograph of scale model tested by helium-gun technique. All linear dimensions are in inches.

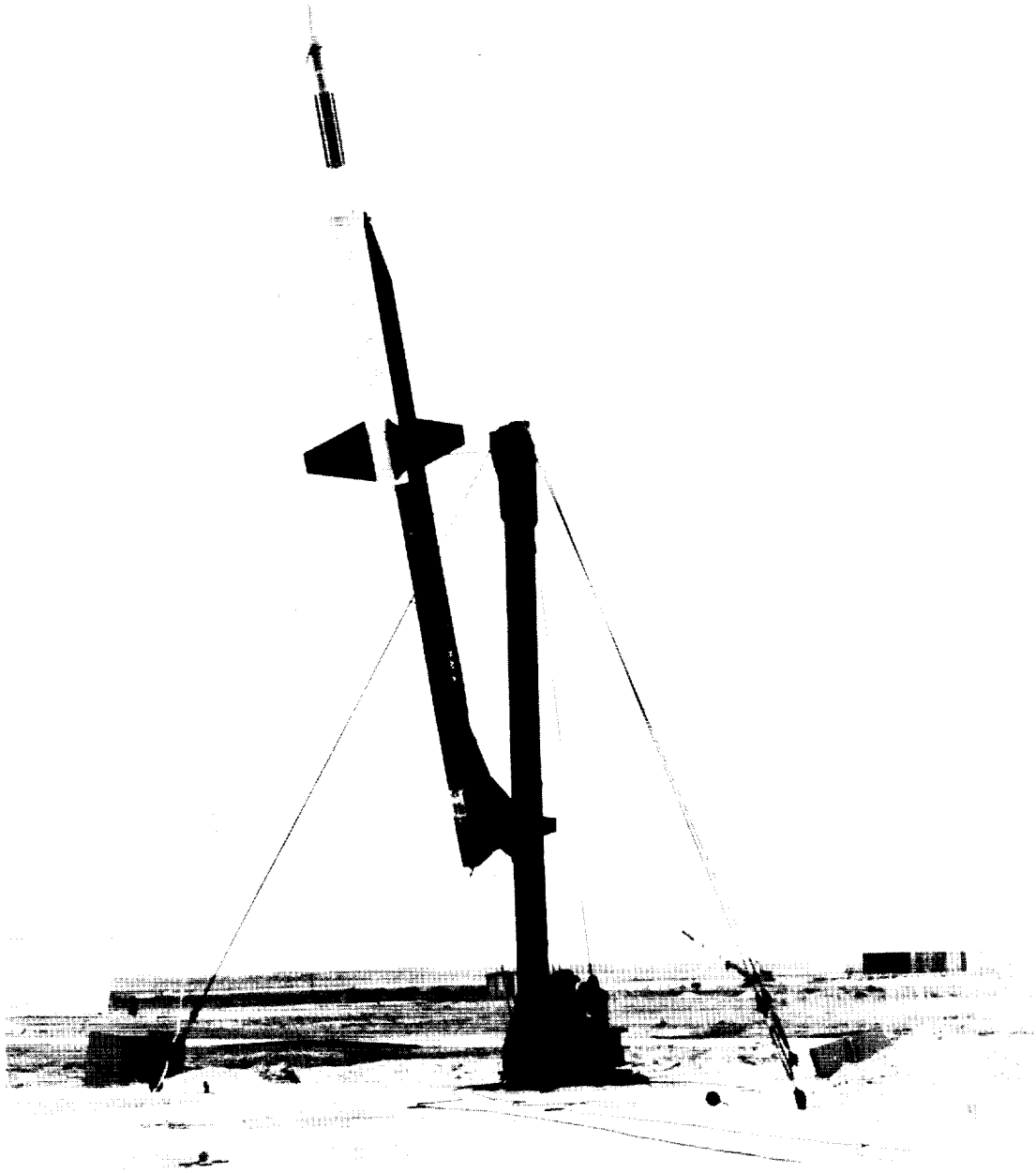

Figure 4.- Model 1 on launcher. L-57-845

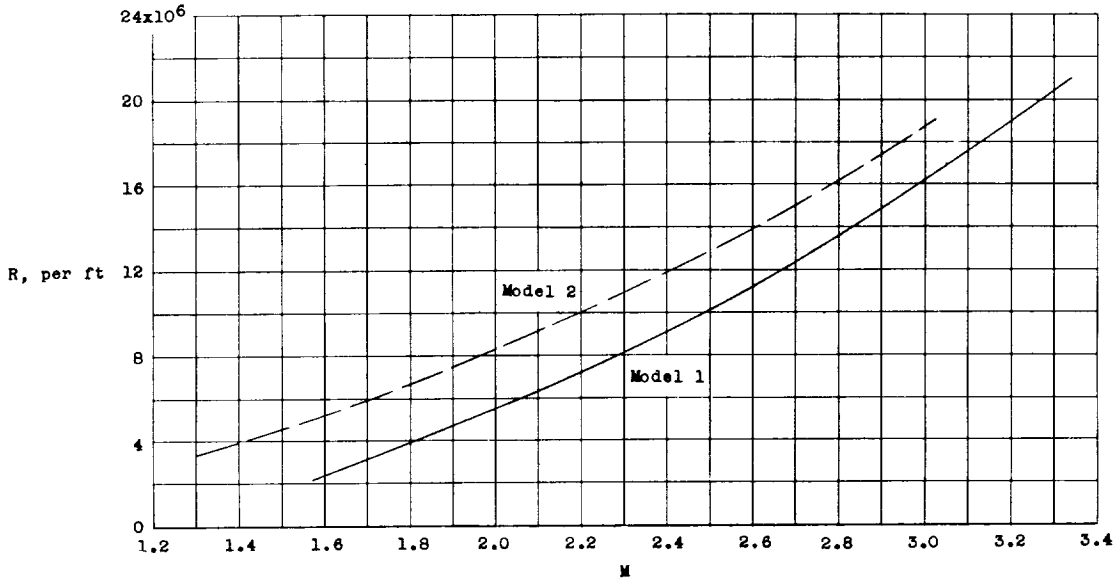

(a) Reynolds number.

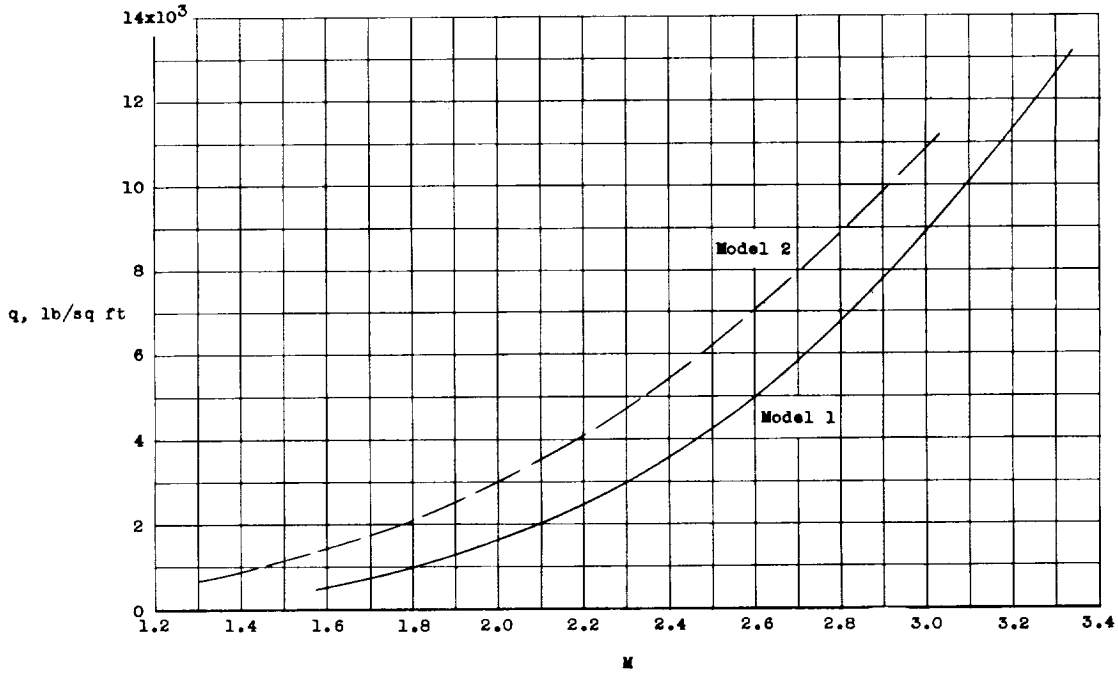

(b) Dynamic pressure.

Figure 5.- Variation of Reynolds number and dynamic pressure with Mach number.

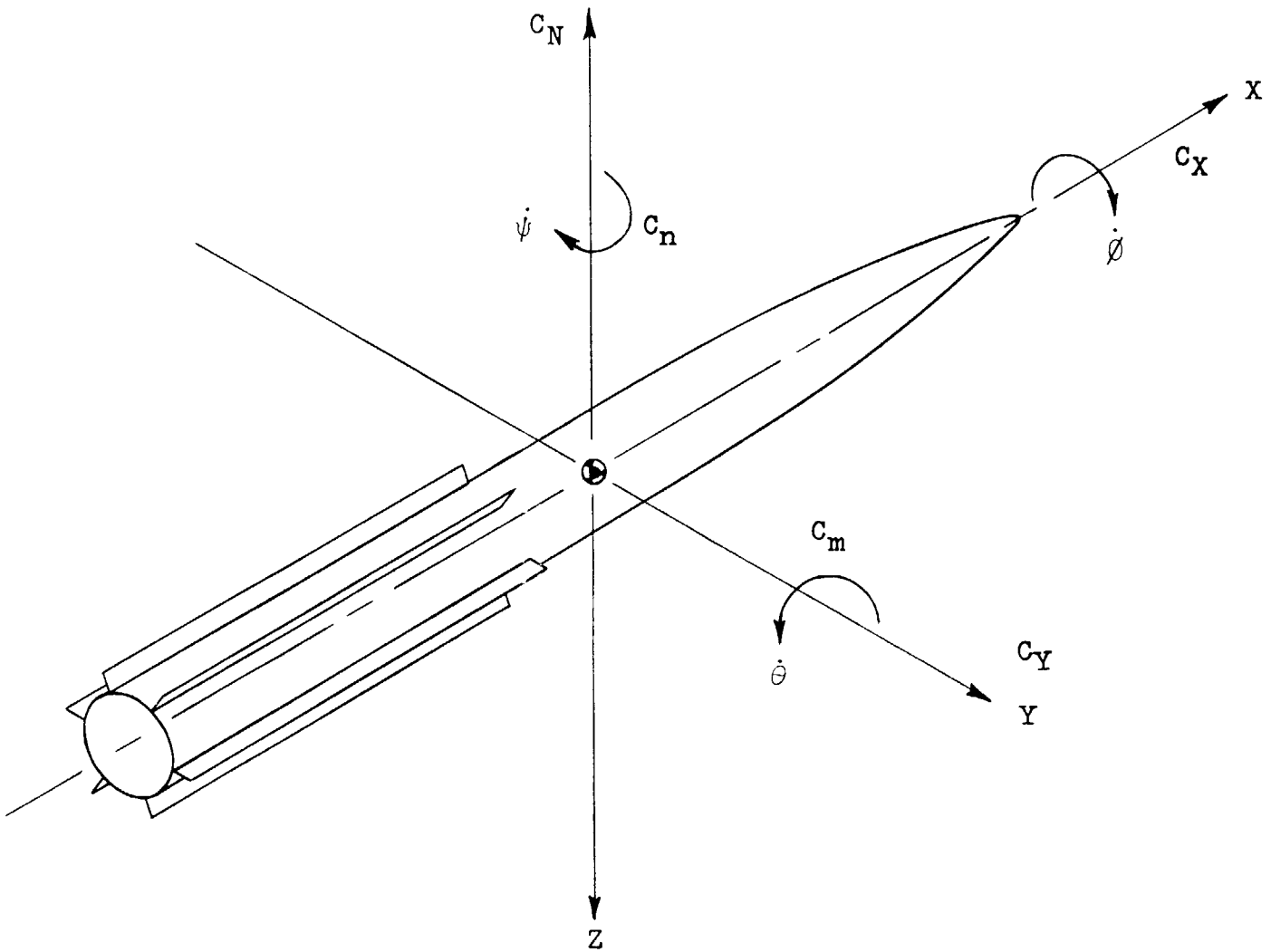

Figure 6.- Coordinate system and sign convention.

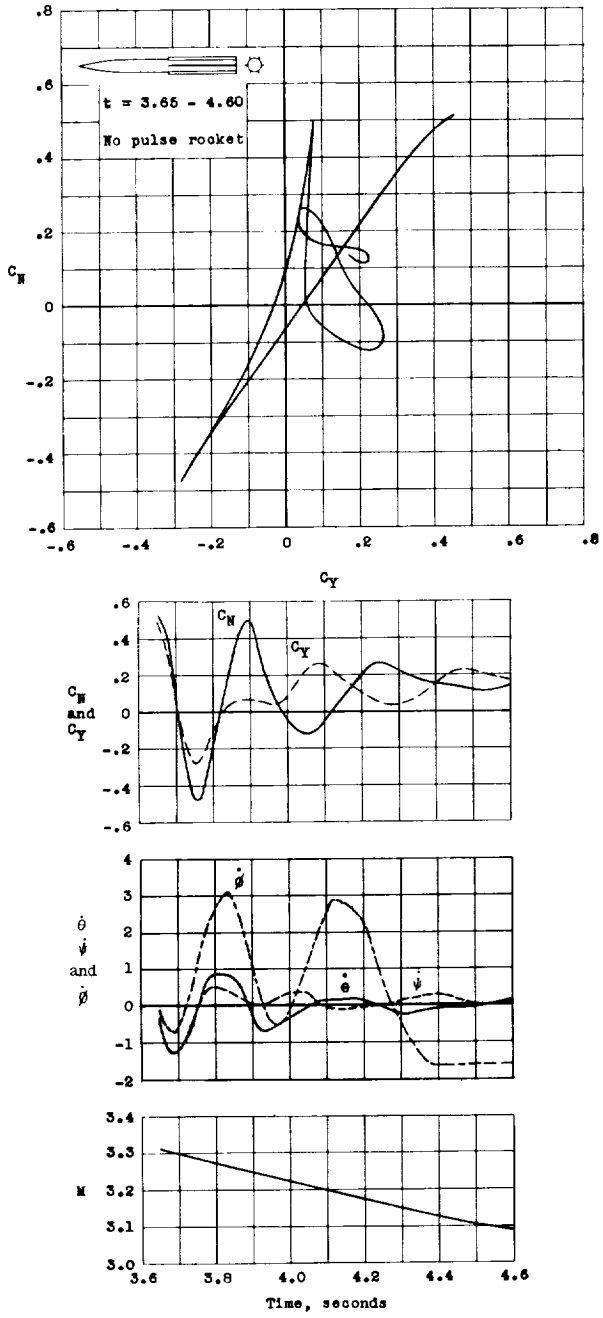

(a) Booster separation pulse.

Figure 7.- Time histories of test flight of model 1.

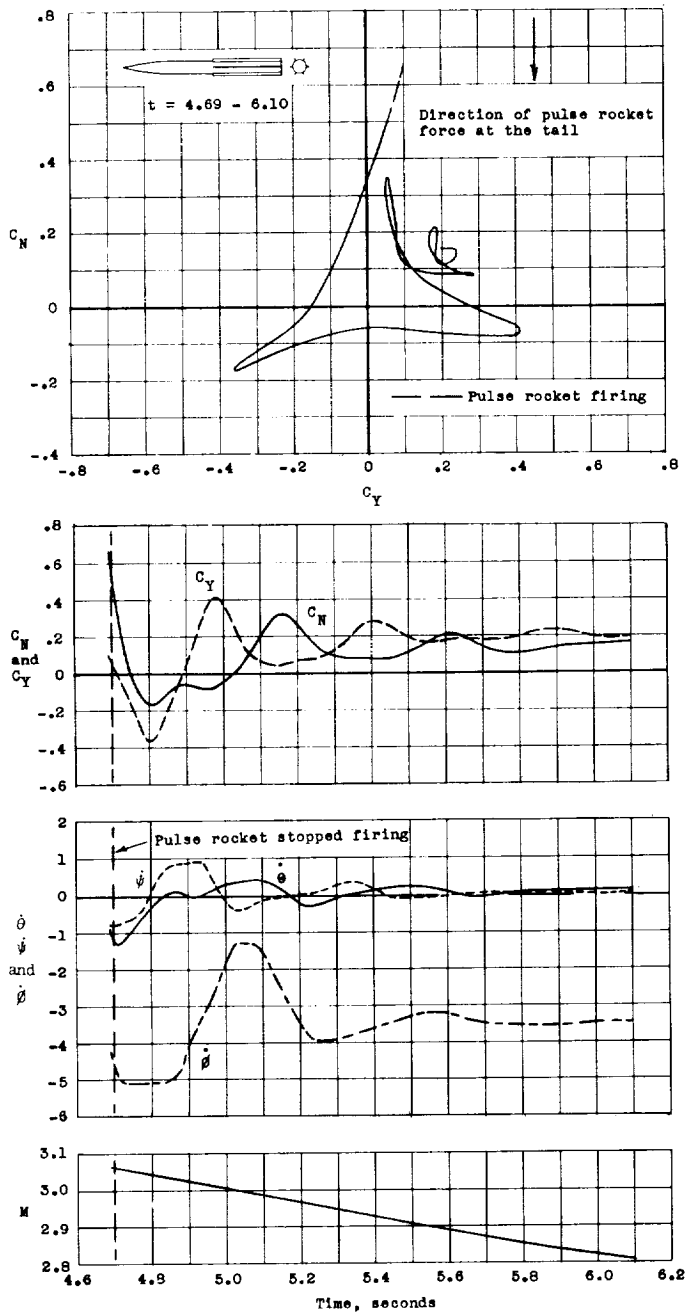

(b) First rocket pulse.

Figure 7.- Continued.

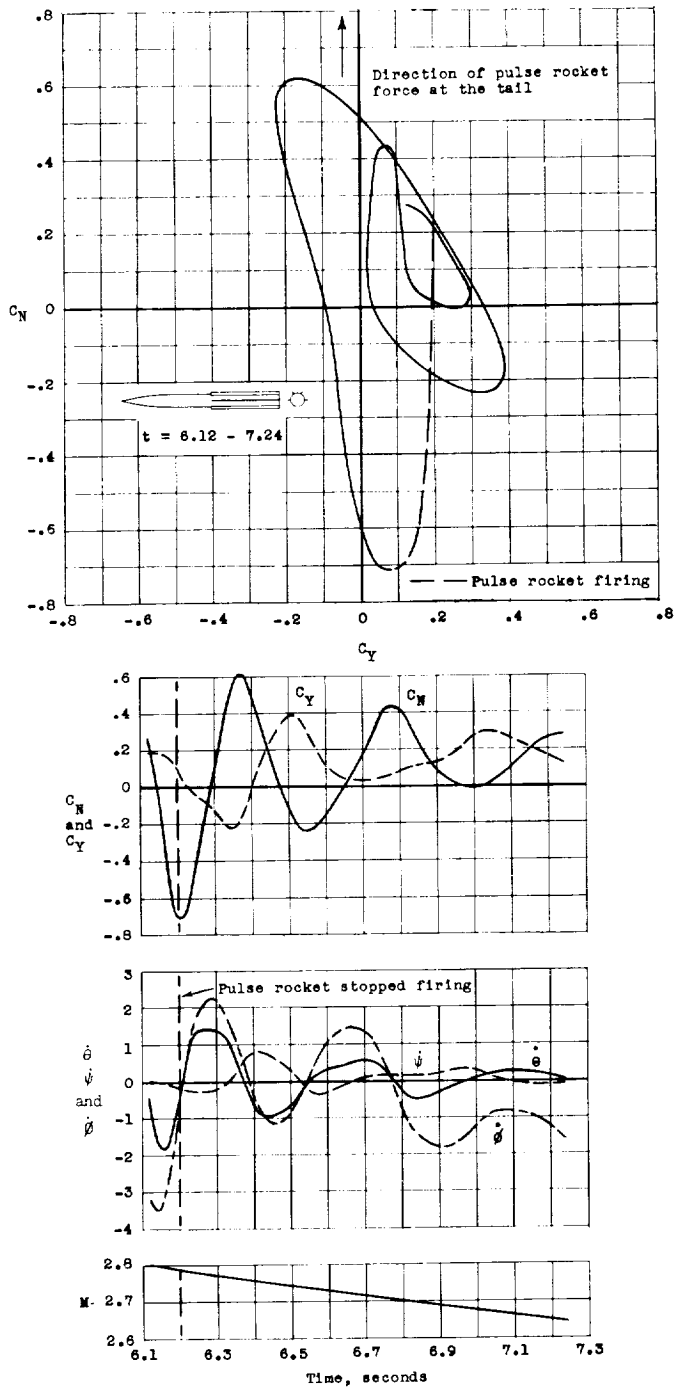

(c) Second rocket pulse.

Figure 7.- Continued.

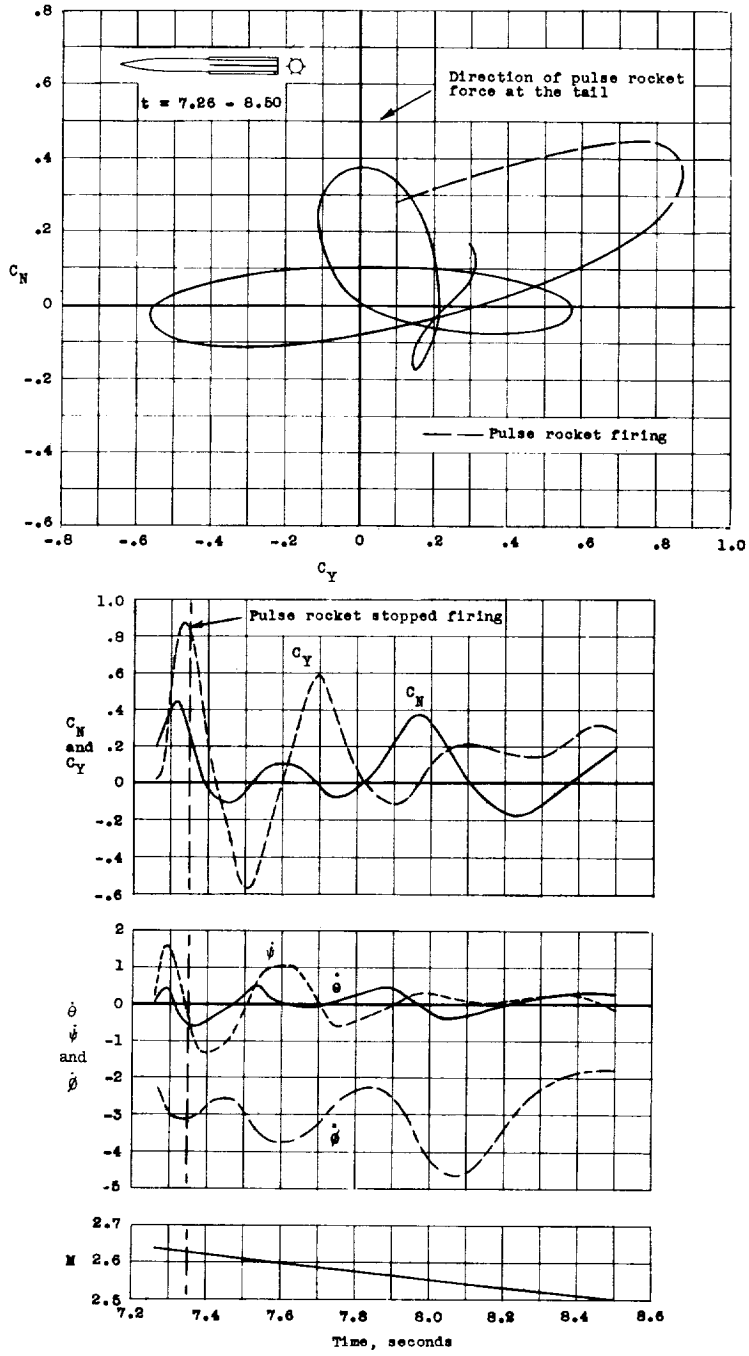

(d) Third rocket pulse.

Figure 7.- Continued.

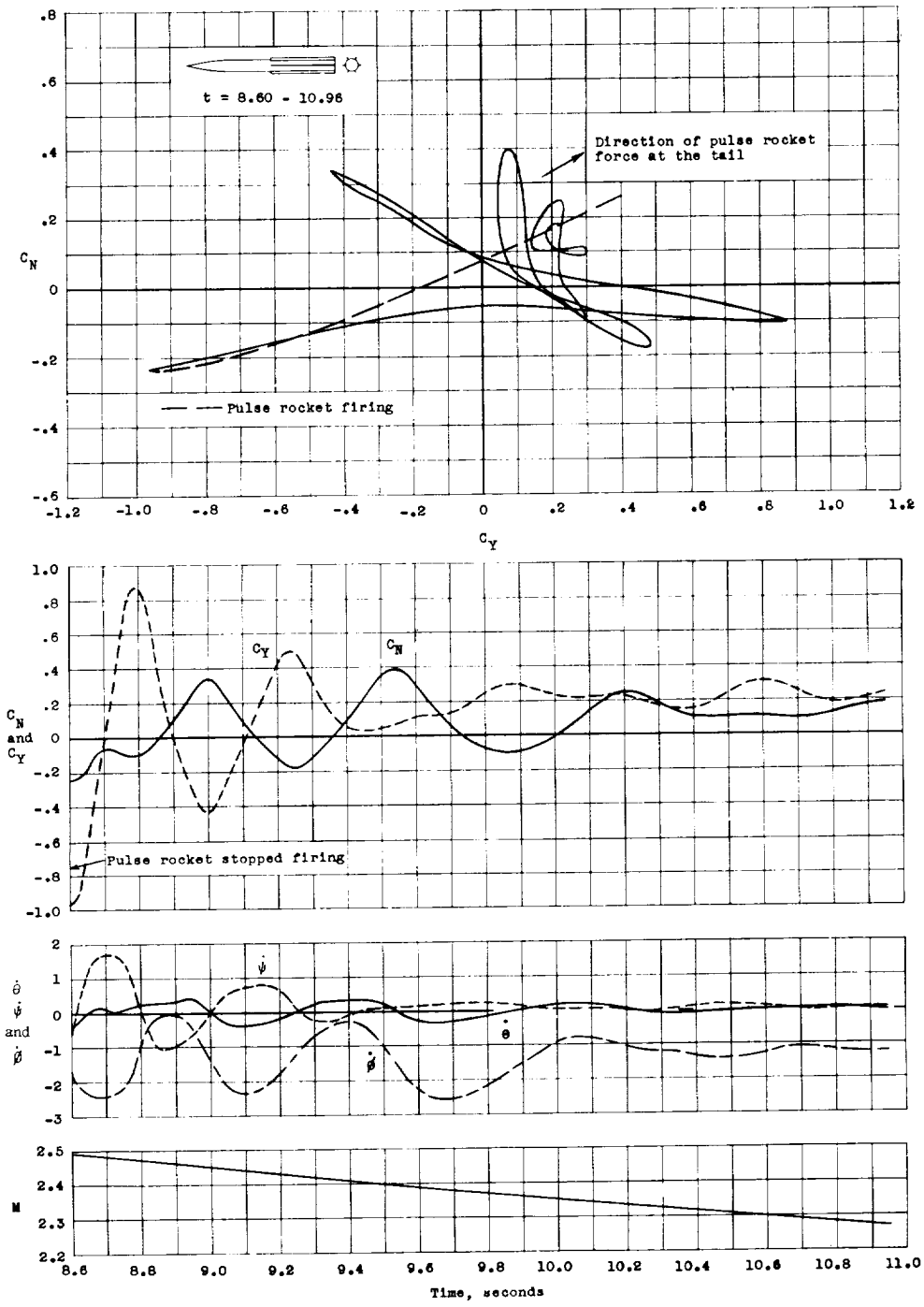

(e) Fourth rocket pulse.

Figure 7.- Continued.

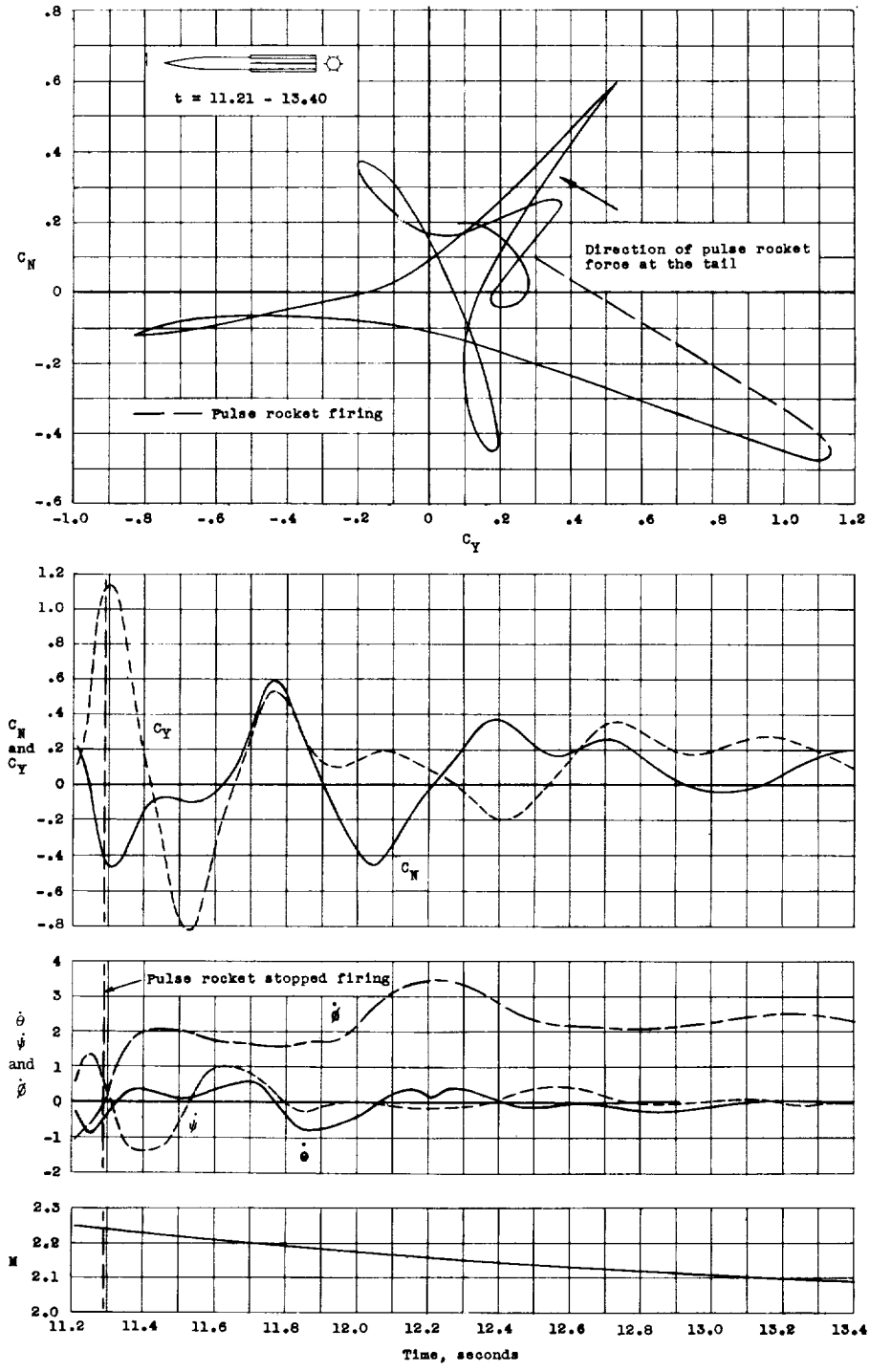

(f) Fifth rocket pulse.

Figure 7.- Continued.

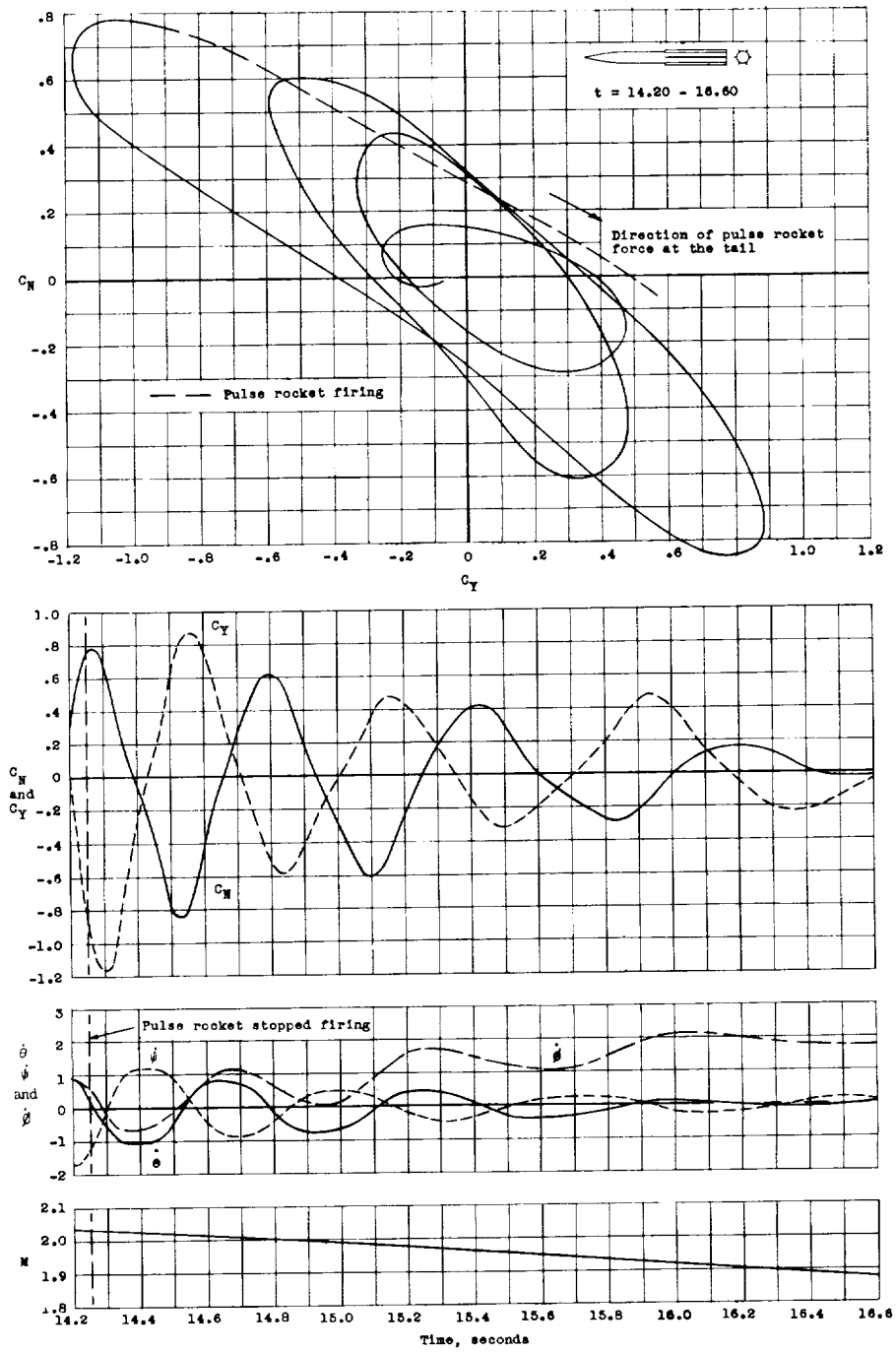

(g) Sixth rocket pulse.

Figure 7.- Concluded.

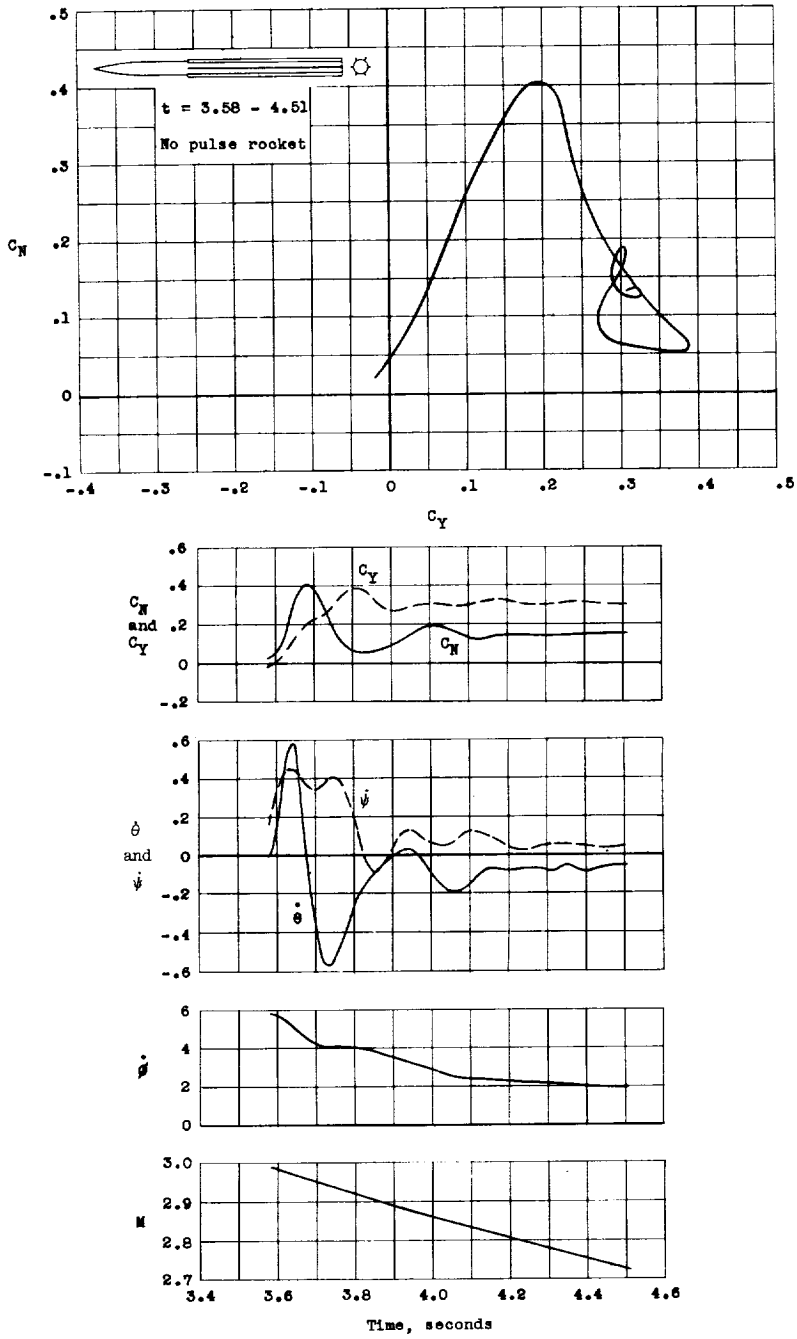

(a) Booster separation pulse.

Figure 8.- Time histories of test flight of model 2.

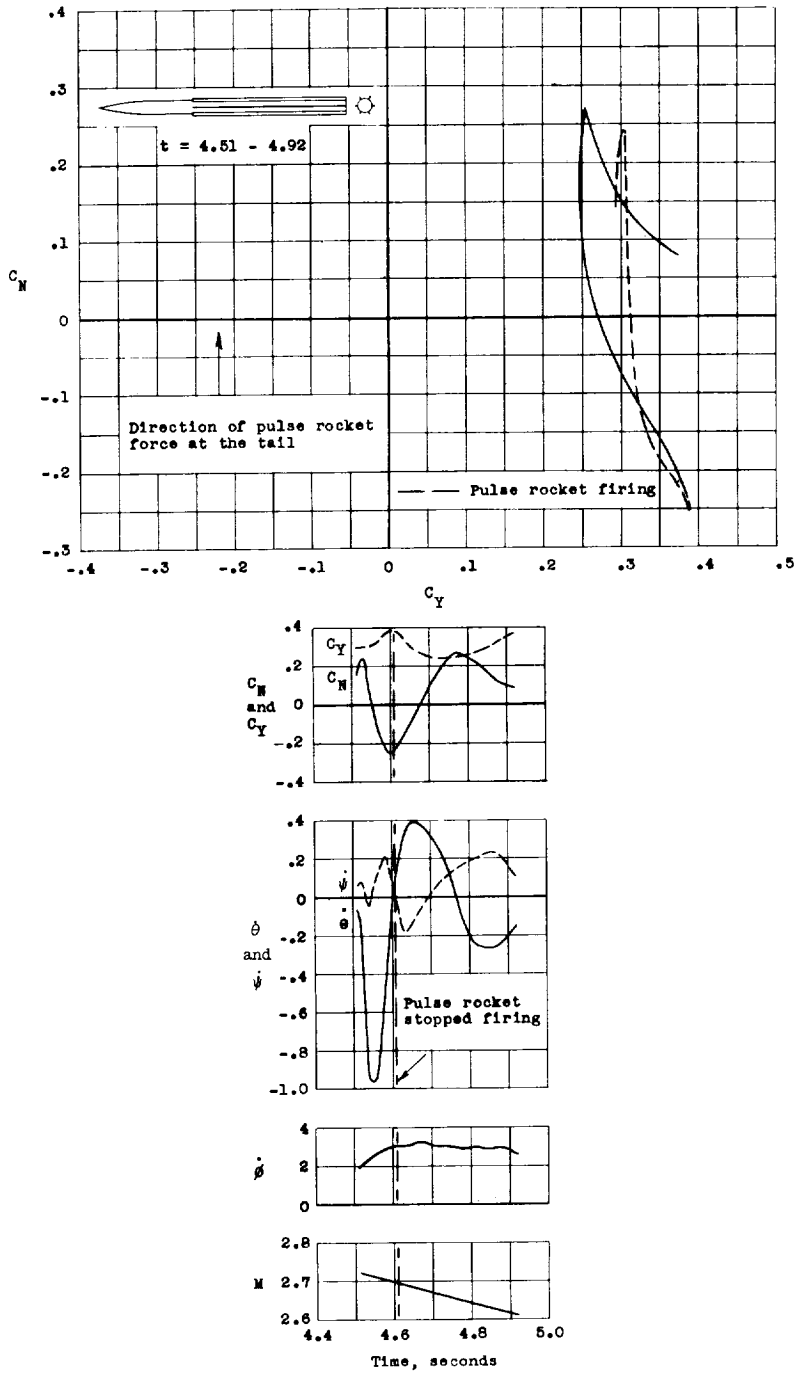

(b) First rocket pulse.

Figure 8.- Continued.

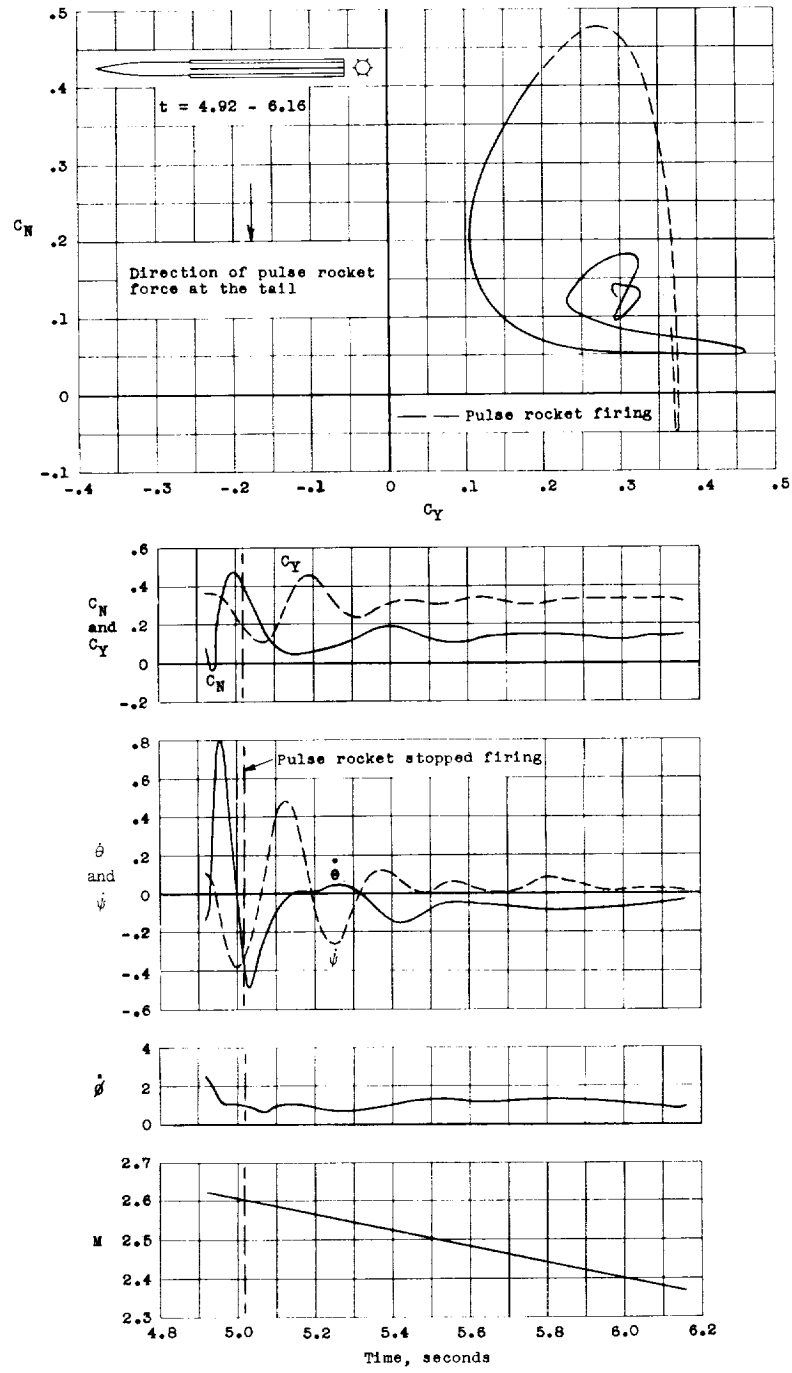

(c) Second rocket pulse.

Figure 8.- Continued.

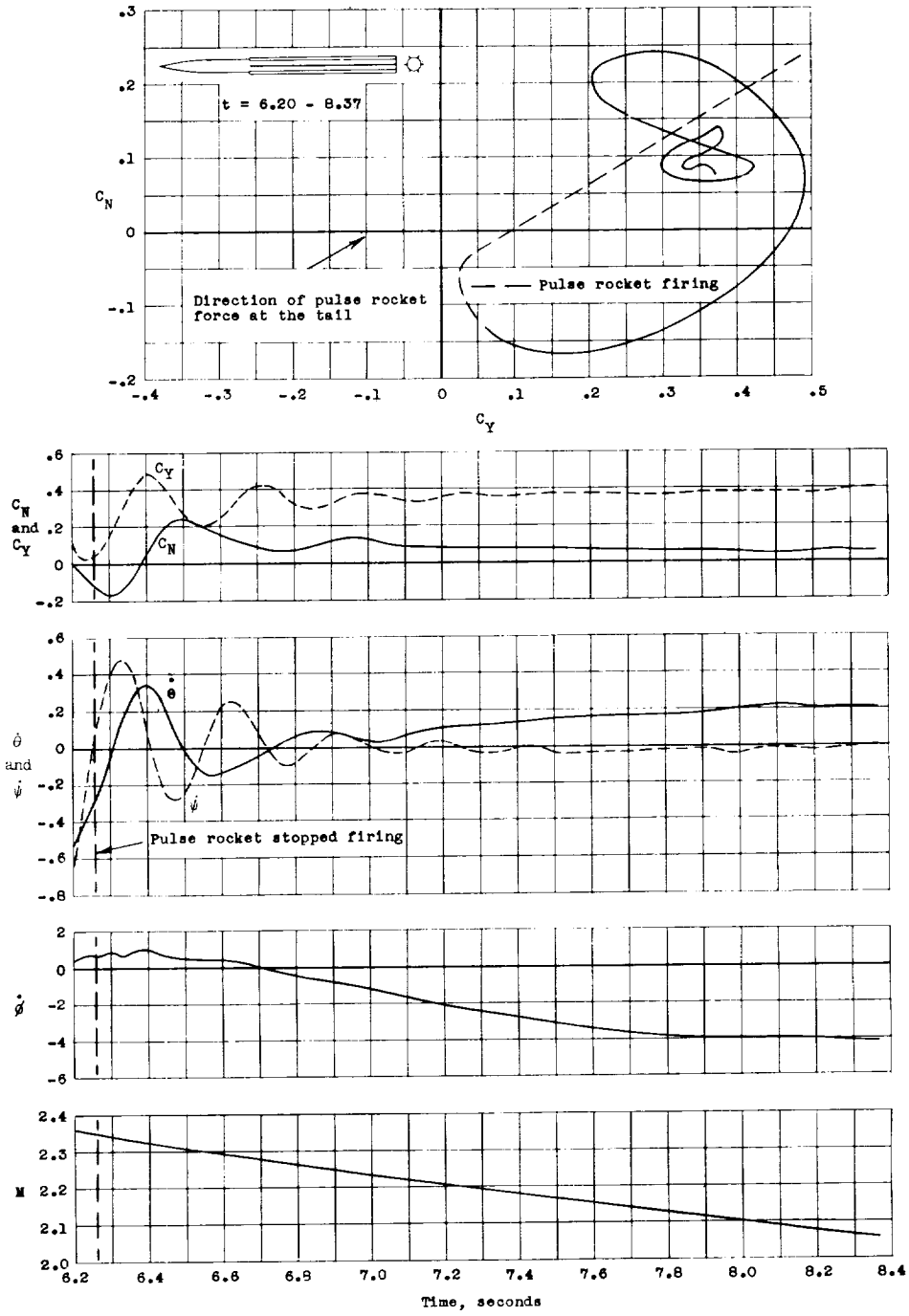

(d) Third rocket pulse.

Figure 8.- Continued.

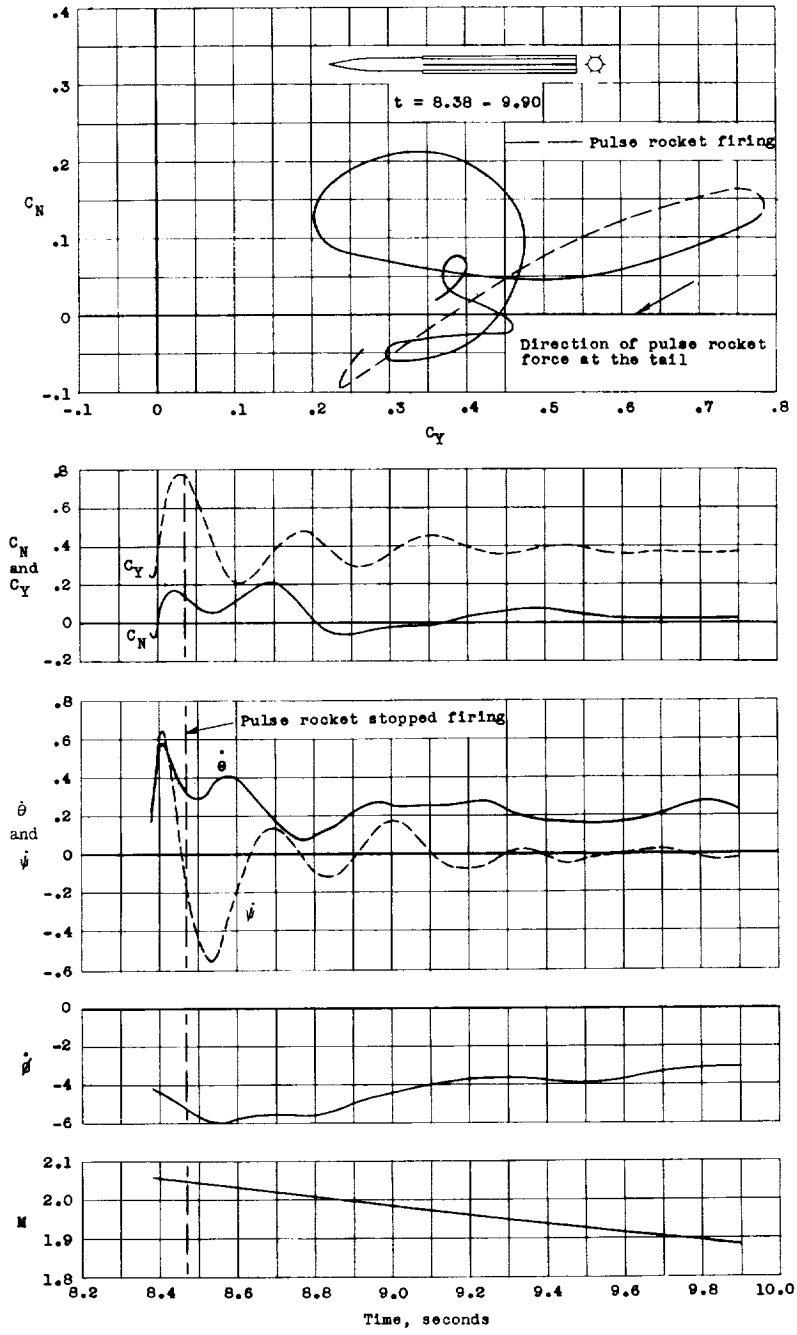

(e) Fourth rocket pulse.

Figure 8.- Continued.

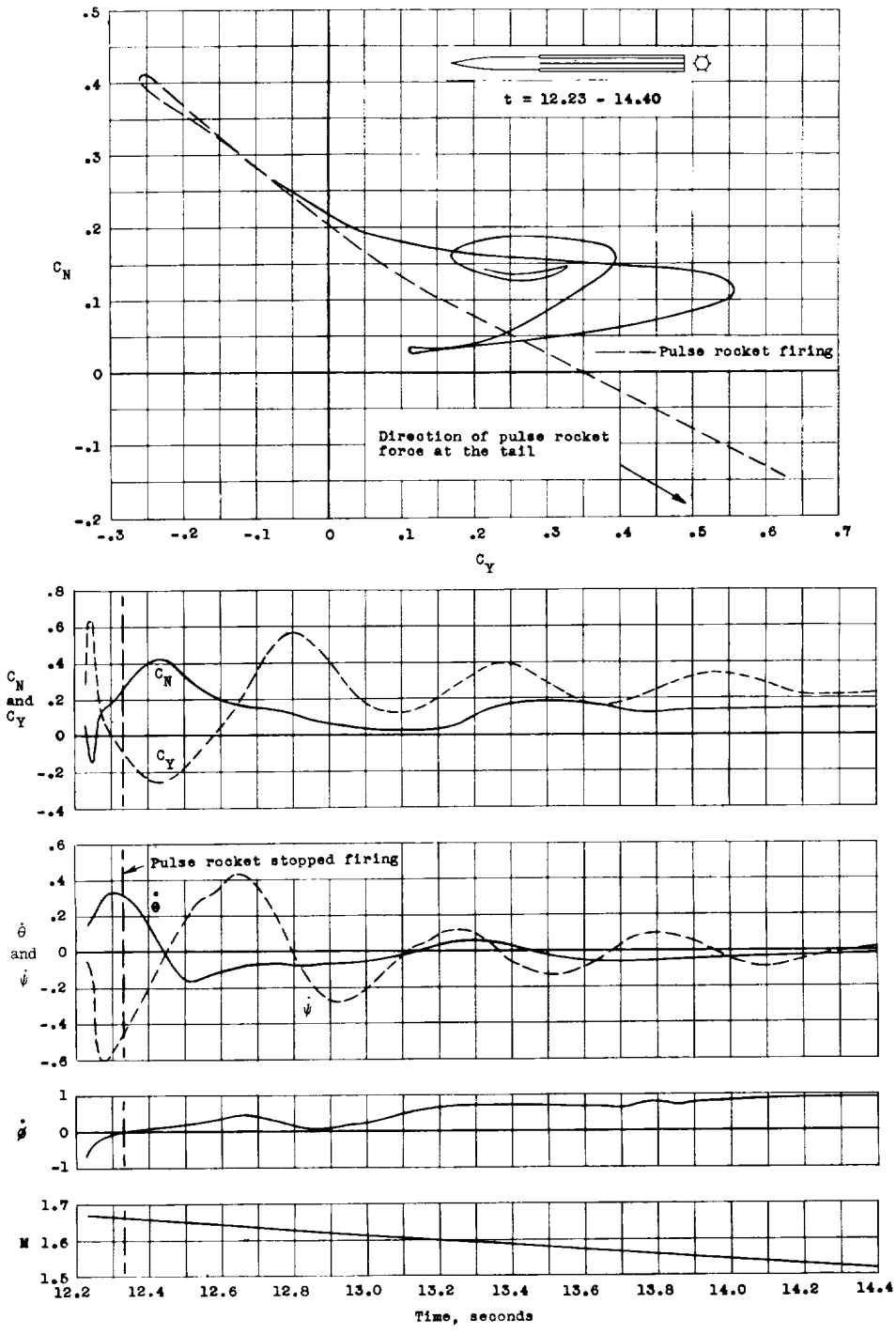

(f) Fifth rocket pulse.

Figure 8.- Continued.

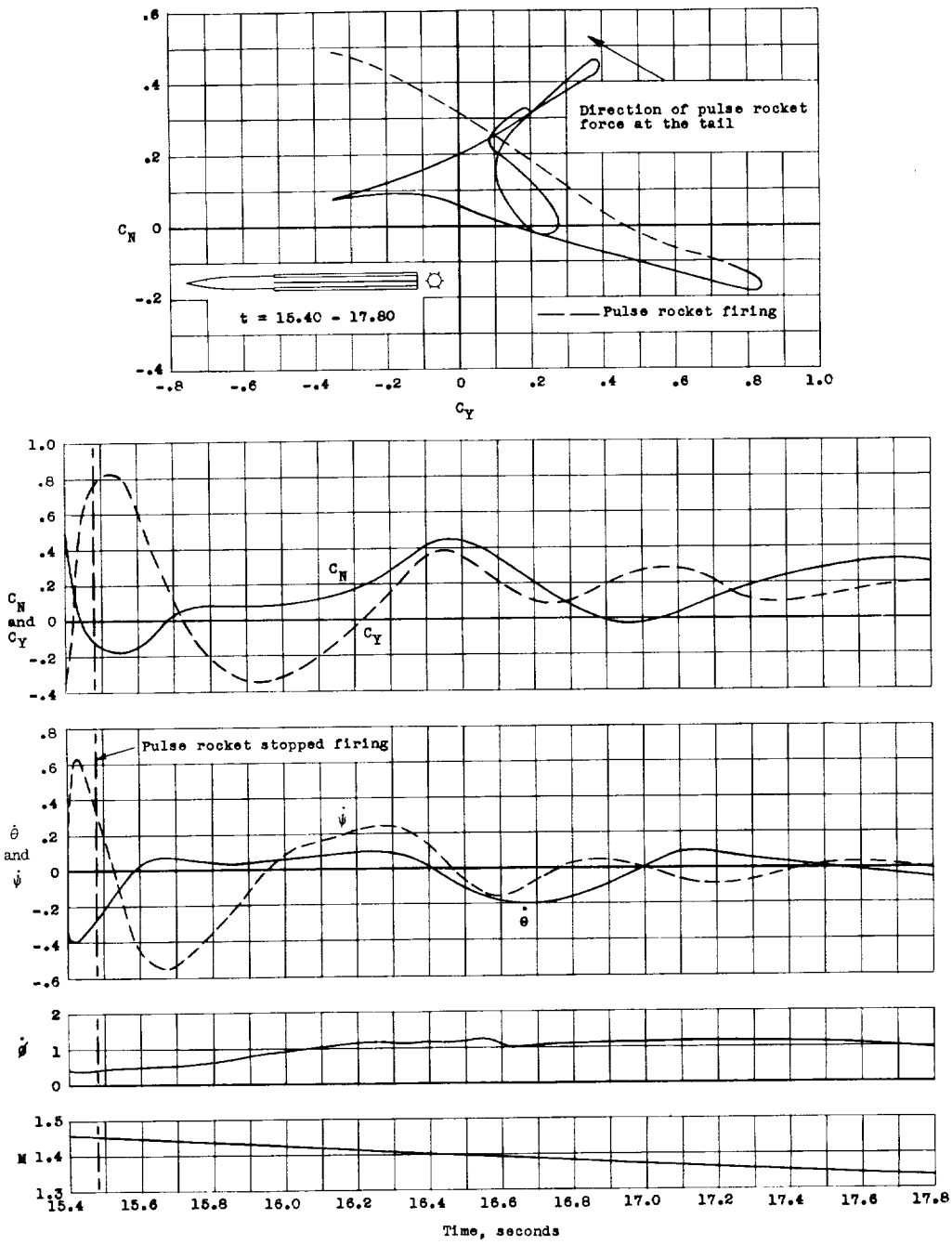

(g) Sixth rocket pulse.

Figure 8.- Concluded.

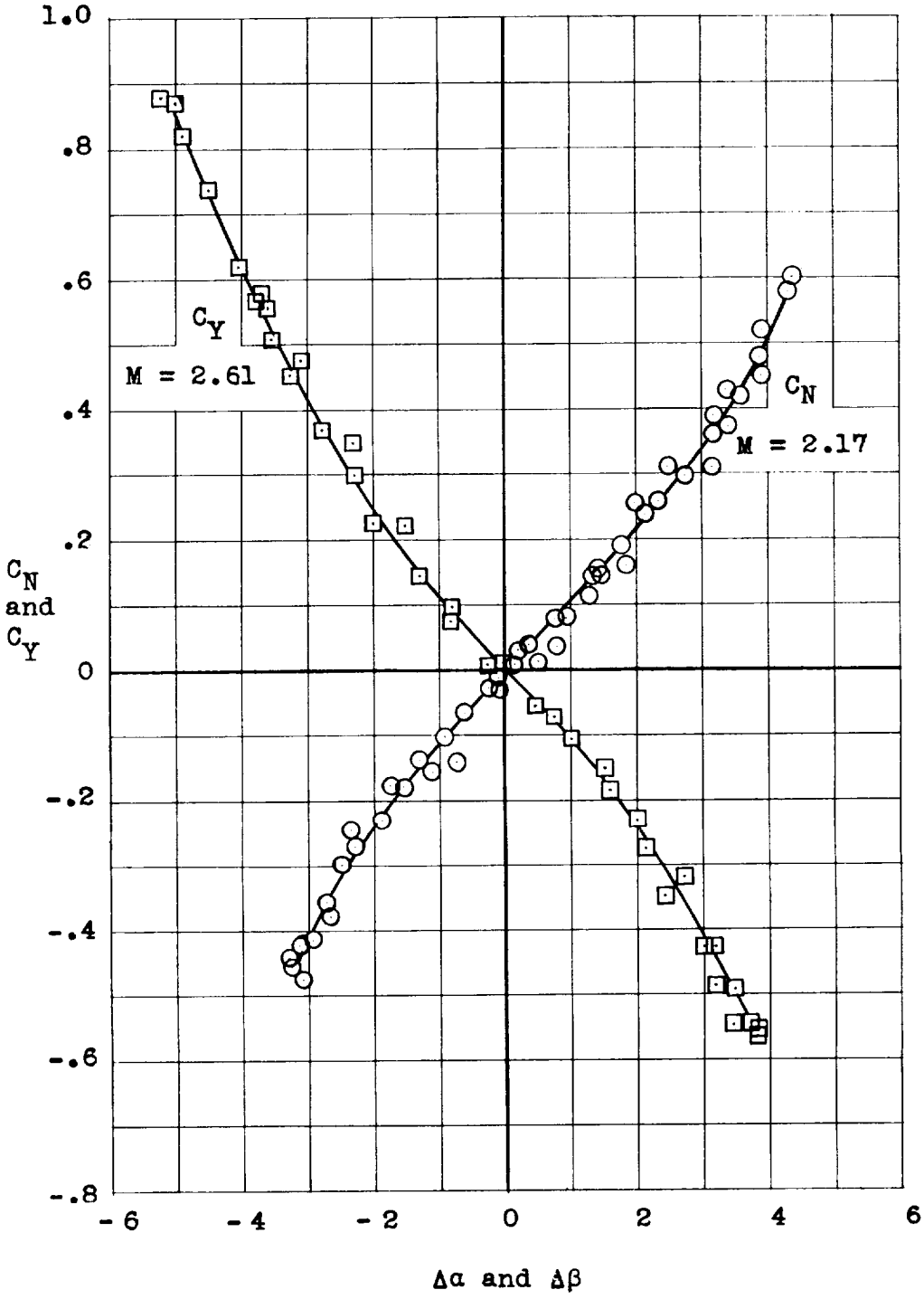

Figure 9.- Typical variation of C_N and C_Y with $\Delta\alpha$ and $\Delta\beta$, respectively, for model 1.

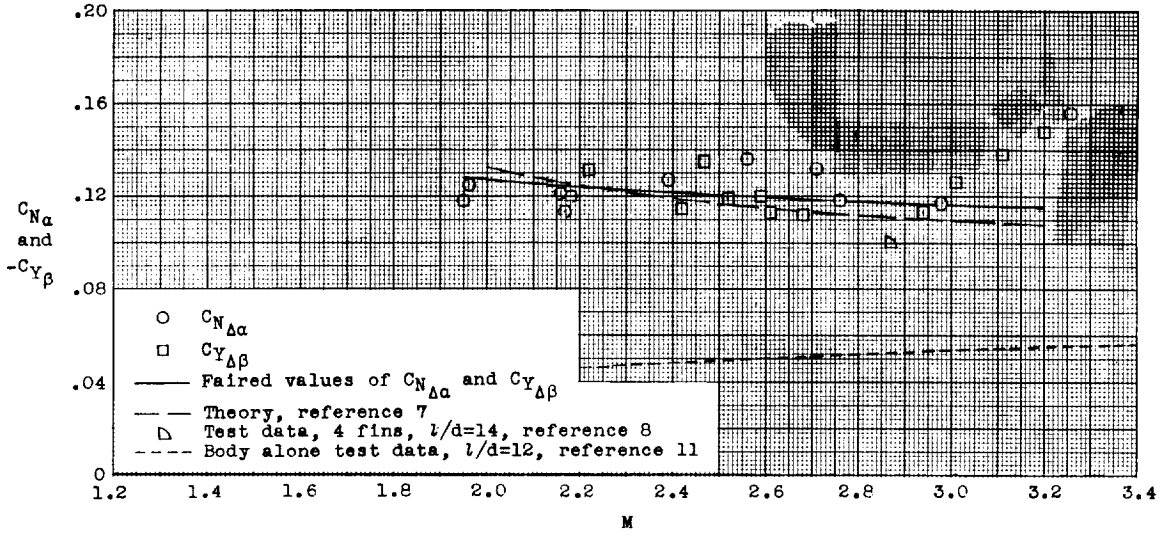

(a) Model 1.

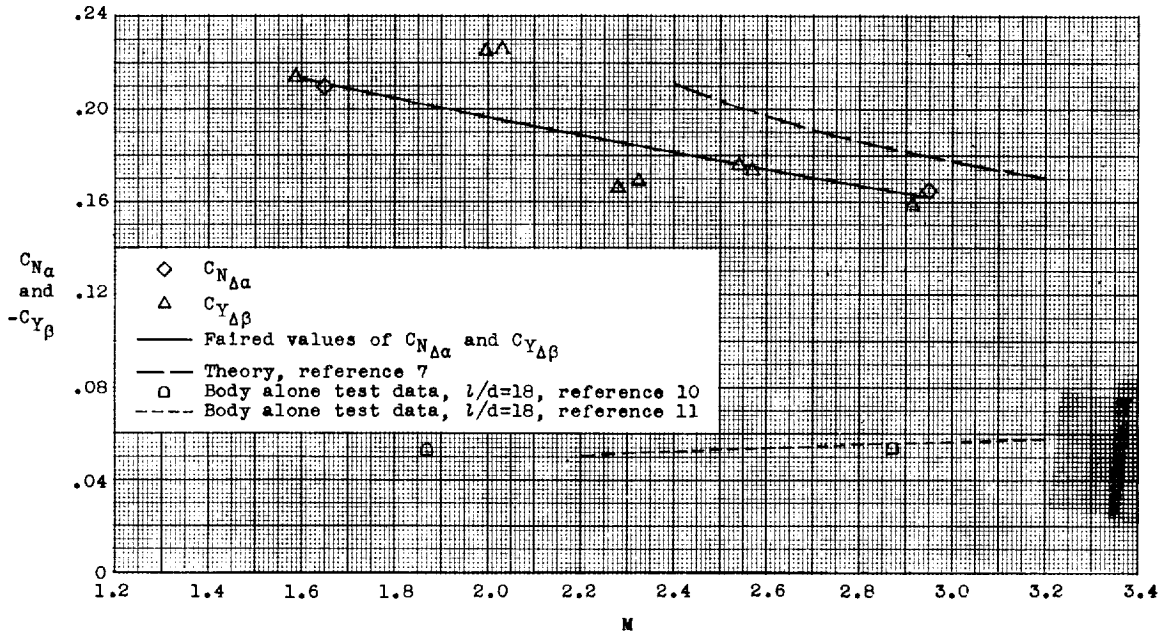

(b) Model 2.

Figure 10.- Variation of normal-force-curve slope and side-force-curve slope with Mach number. Reference data included from theory and body-alone tests.

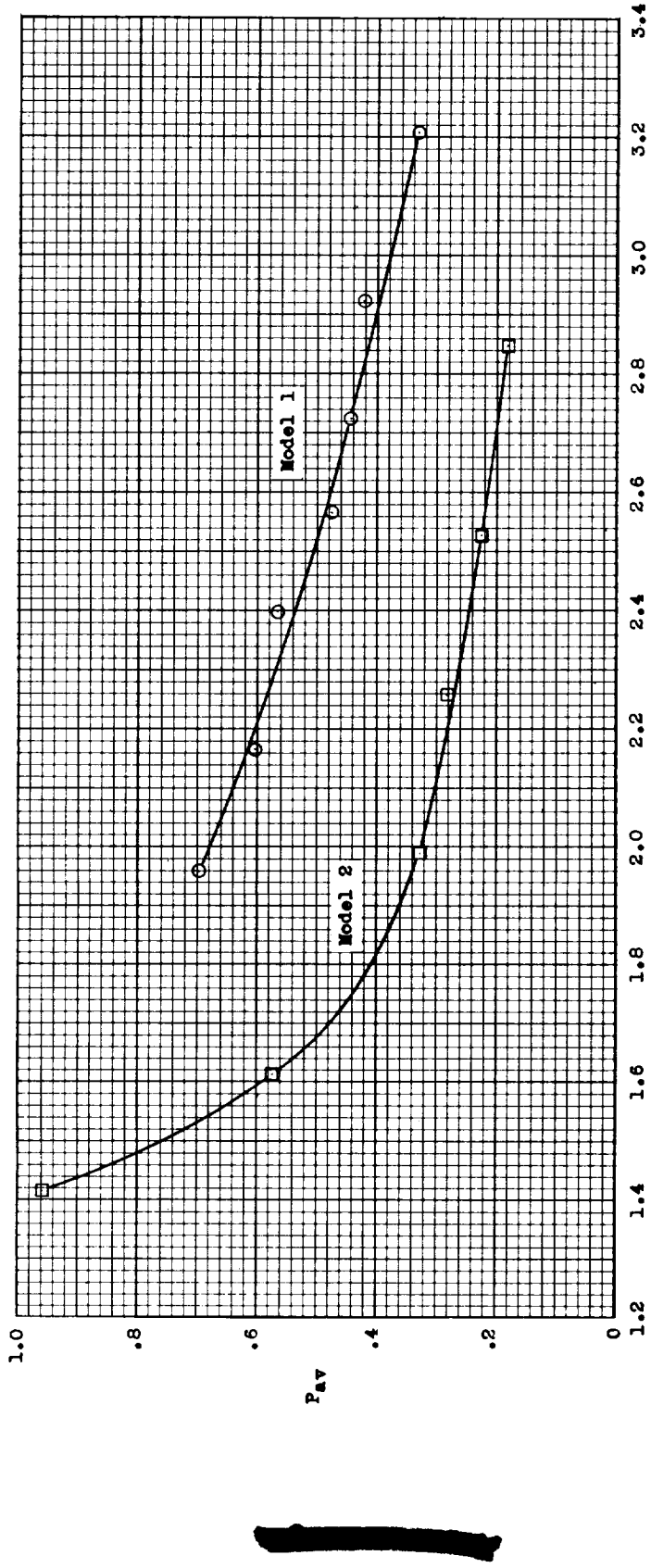

Figure 11.- Variation of average period of oscillation with Mach number for models 1 and 2.

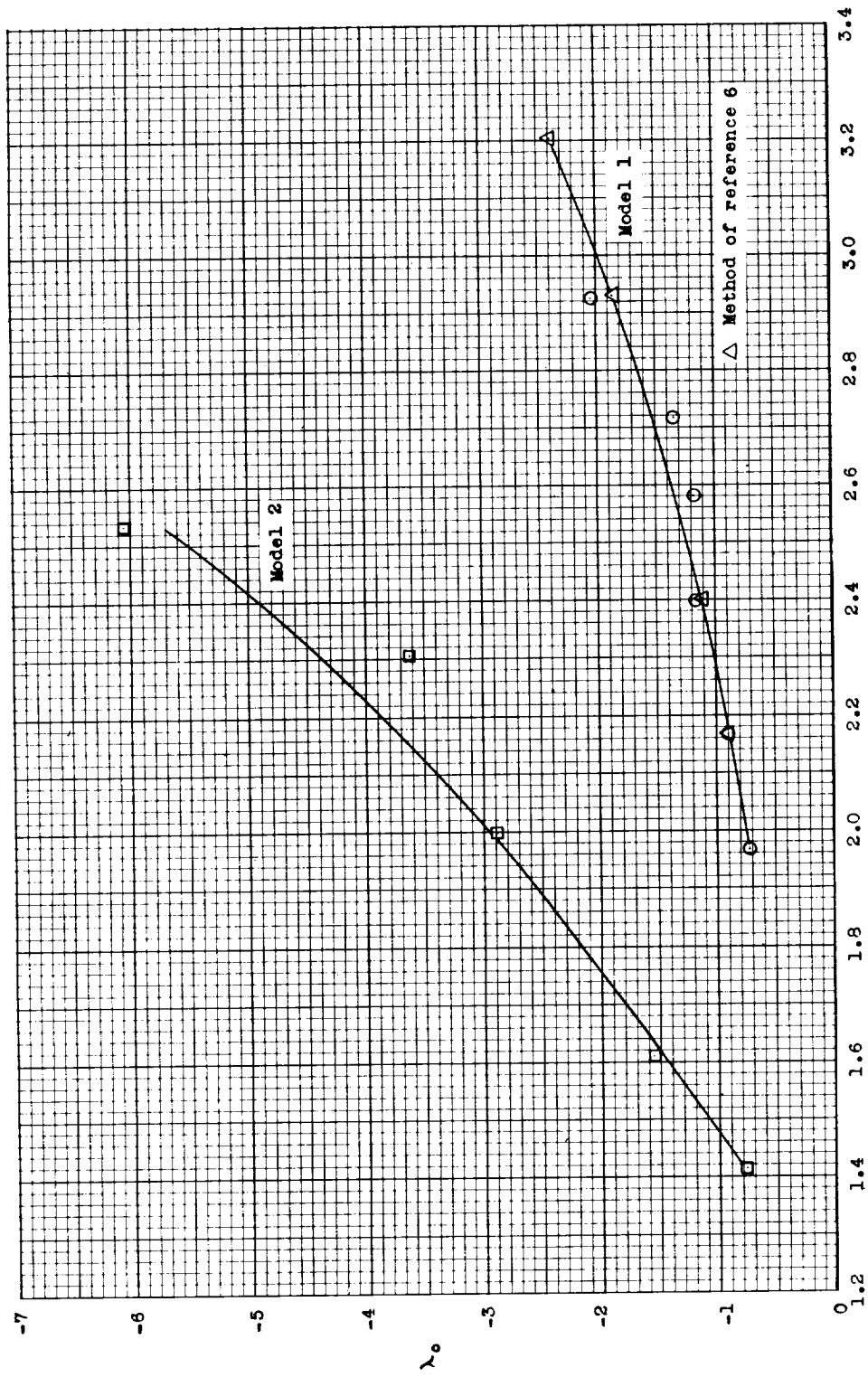

Figure 12.- Variation of exponential damping constant with Mach number for models 1 and 2.

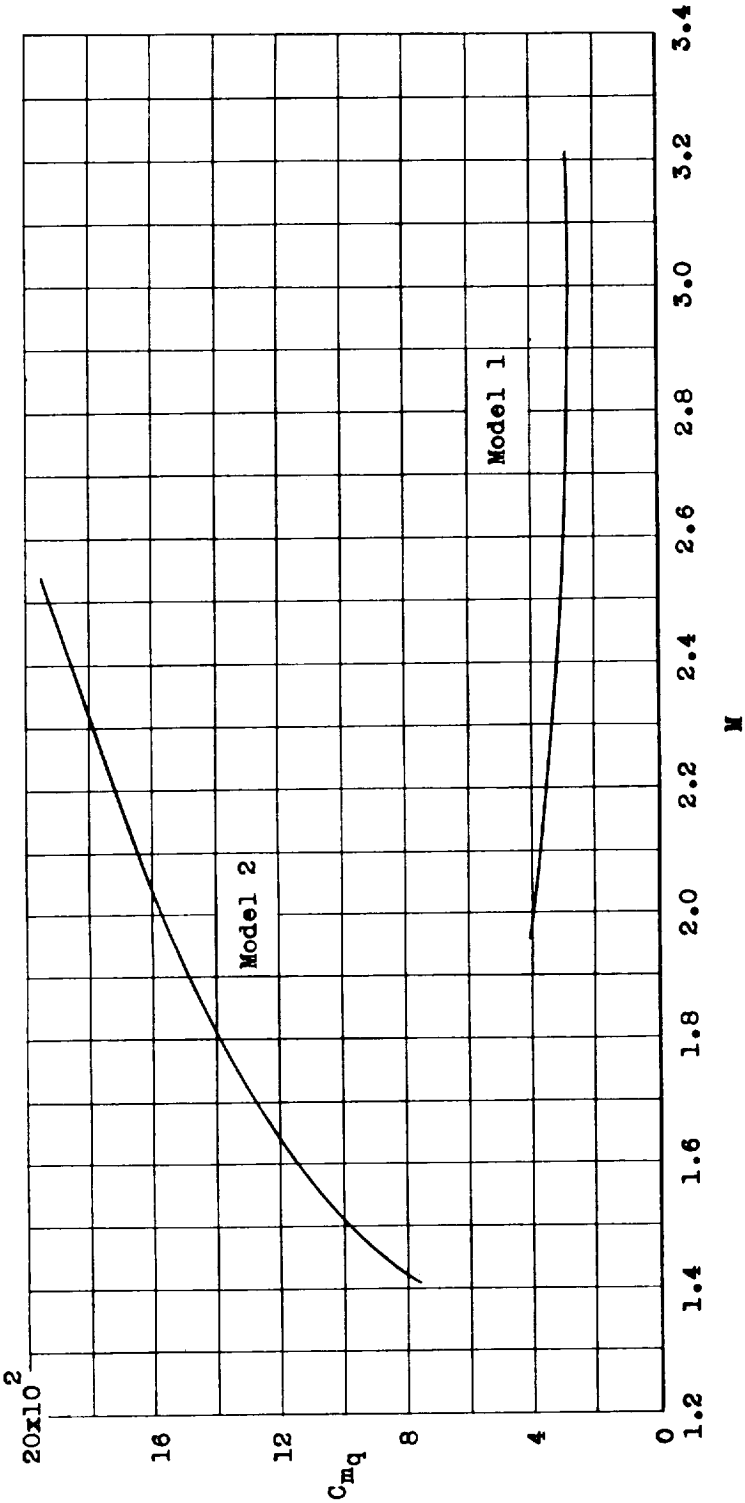

Figure 13.- Variation of damping derivative C_{m_q} with Mach number for models 1 and 2.

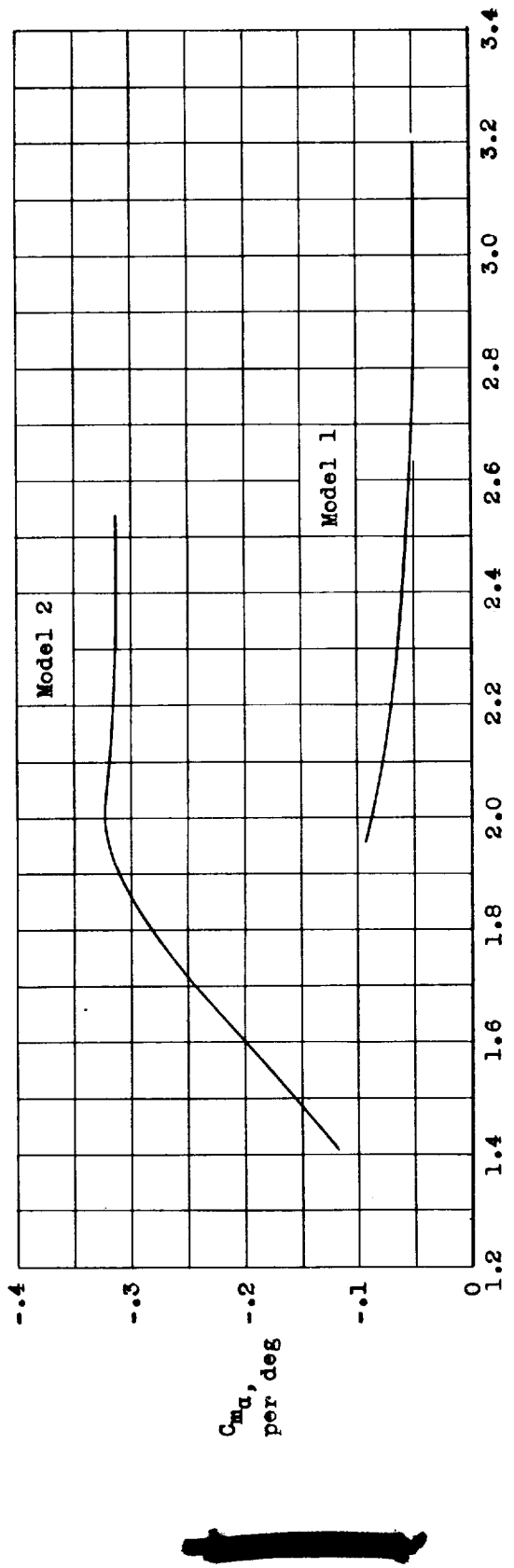

Figure 14.- Variation of static stability derivative with Mach number for models 1 and 2.

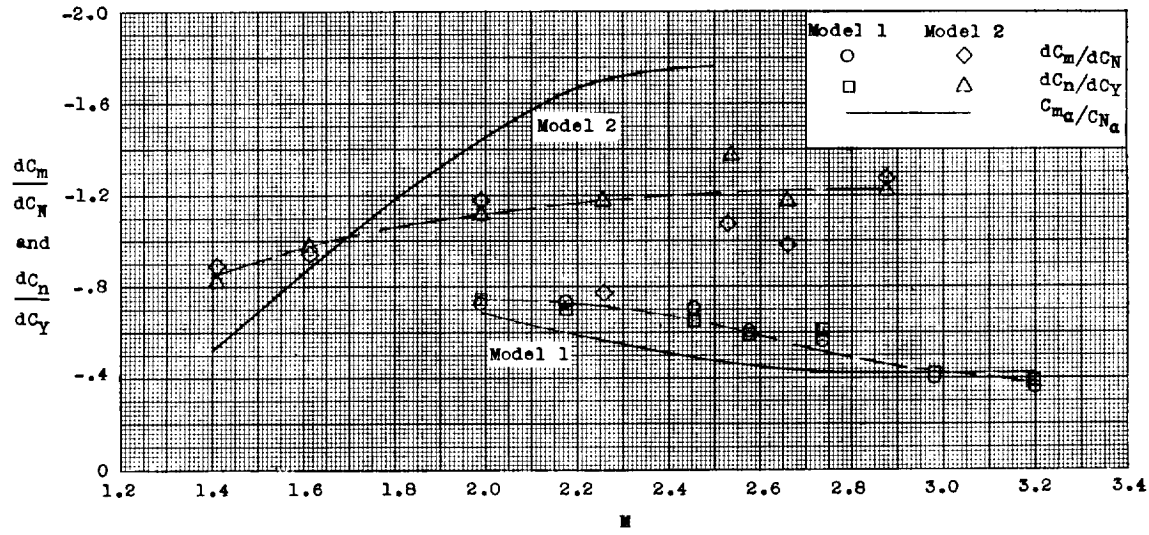

(a) Static margin in body diameters.

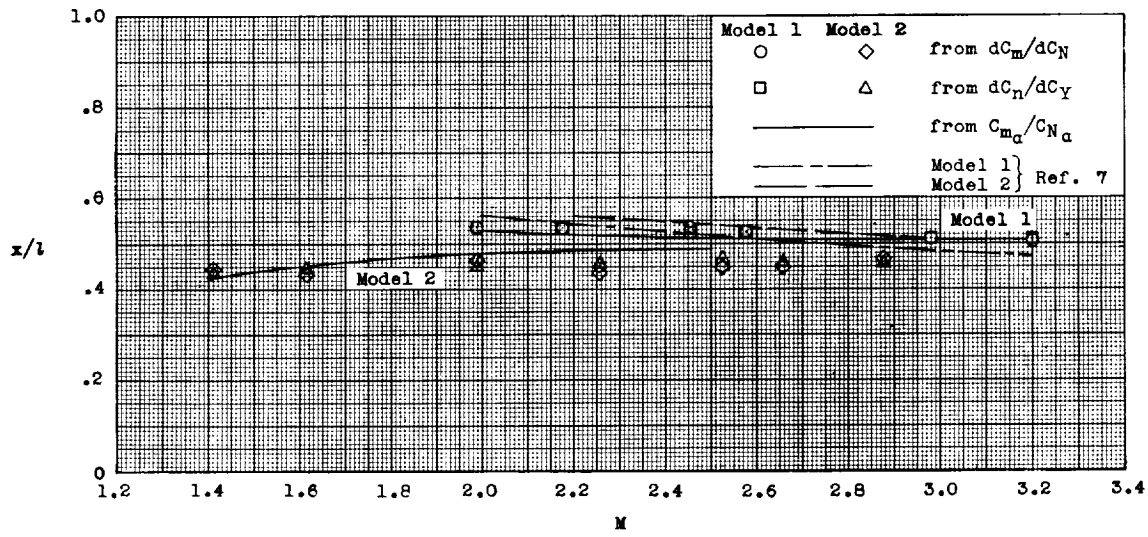

(b) Center of pressure from the nose of the model as a ratio of center-of-pressure location to body length.

Figure 15.- Variation of center of pressure with Mach number for models 1 and 2.

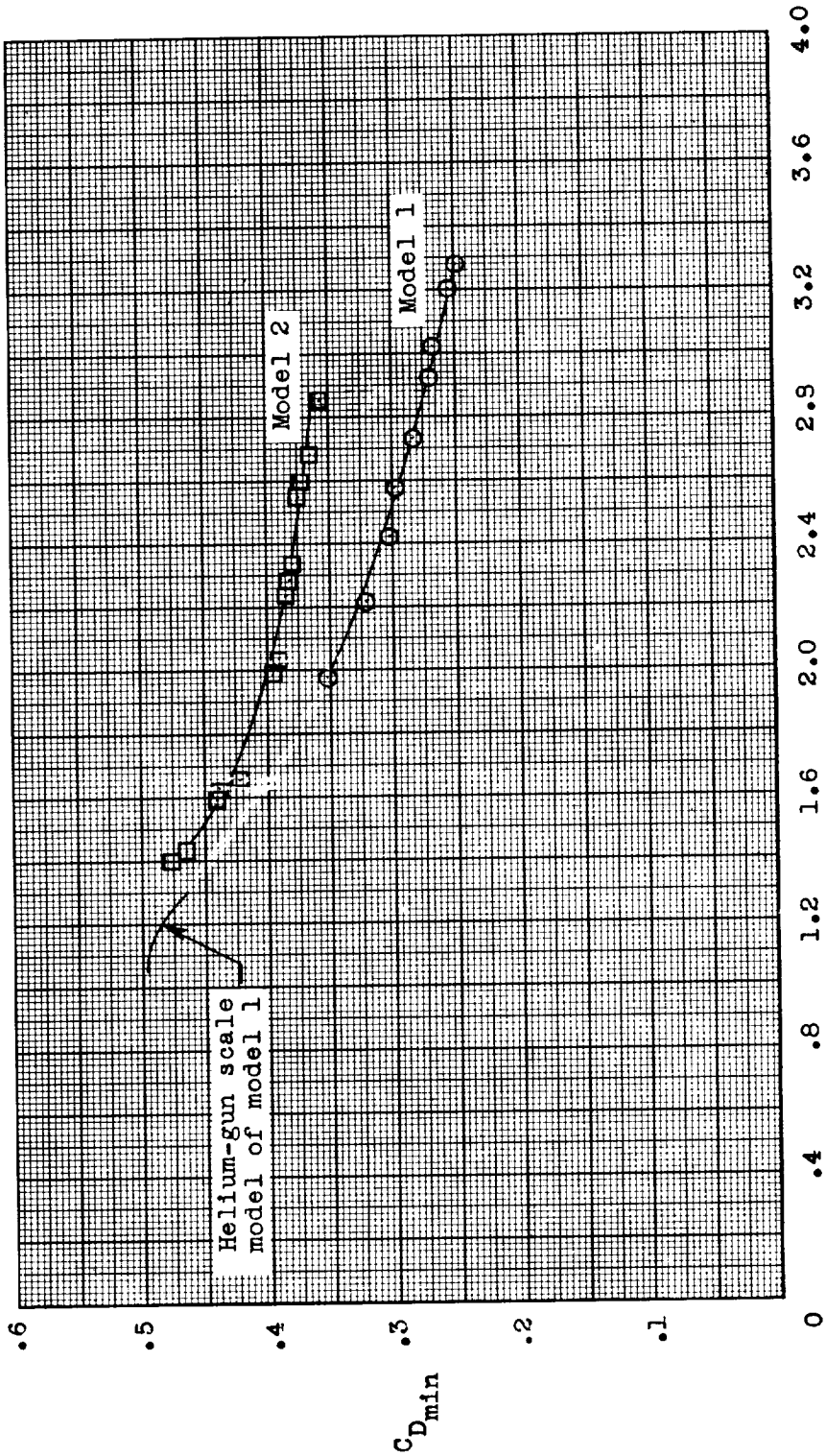

Figure 16.- Variation of minimum drag coefficient of test models with Mach number.

NASA MEMO 12-2-58L
National Aeronautics and Space Administration.
STABILITY CHARACTERISTICS OF TWO MISSILES OF FINENESS RATIOS 12 AND 18 WITH SIX RECTANGULAR FINS OF VERY LOW ASPECT RATIO OVER A MACH NUMBER RANGE OF 1.4 TO 3.2.
Allen B. Henning. January 1959. 48p. diagrs., photos., tabs. (NASA MEMORANDUM 12-2-58L)

(Title, Unclassified)

The missiles were flight tested and were disturbed in flight by six pulse rockets over a Reynolds number range of 2×10^6 to 21×10^6. These free-flight missiles experienced little induced roll. Extending the body and fins of the shorter missile six diameters changed the fin aspect ratio from approximately 0.04 to approximately 0.02 and increased the value of the lift-curve slope, the dynamic stability, and the drag.

Copies obtainable from NASA, Washington

[redacted]

1. Missiles - Components in Combination (1.7.2.1)
2. Stability, Static (1.8.1.1)
3. Stability, Dynamic (1.8.1.2)
4. Mass and Gyroscopic Problems (1.8.6)

I. Henning, Allen B.
II. NASA MEMO 12-2-58L

NASA

[redacted]

NASA MEMO 12-2-58L
National Aeronautics and Space Administration.
STABILITY CHARACTERISTICS OF TWO MISSILES OF FINENESS RATIOS 12 AND 18 WITH SIX RECTANGULAR FINS OF VERY LOW ASPECT RATIO OVER A MACH NUMBER RANGE OF 1.4 TO 3.2.
Allen B. Henning. January 1959. 48p. diagrs., photos., tabs. (NASA MEMORANDUM 12-2-58L)

(Title, Unclassified)

The missiles were flight tested and were disturbed in flight by six pulse rockets over a Reynolds number range of 2×10^6 to 21×10^6. These free-flight missiles experienced little induced roll. Extending the body and fins of the shorter missile six diameters changed the fin aspect ratio from approximately 0.04 to approximately 0.02 and increased the value of the lift-curve slope, the dynamic stability, and the drag.

Copies obtainable from NASA, Washington

[redacted]

1. Missiles - Components in Combination (1.7.2.1)
2. Stability, Static (1.8.1.1)
3. Stability, Dynamic (1.8.1.2)
4. Mass and Gyroscopic Problems (1.8.6)

I. Henning, Allen B.
II. NASA MEMO 12-2-58L

NASA

[redacted]

NASA MEMO 12-2-58L
National Aeronautics and Space Administration.
STABILITY CHARACTERISTICS OF TWO MISSILES OF FINENESS RATIOS 12 AND 18 WITH SIX RECTANGULAR FINS OF VERY LOW ASPECT RATIO OVER A MACH NUMBER RANGE OF 1.4 TO 3.2.
Allen B. Henning. January 1959. 48p. diagrs., photos., tabs. (NASA MEMORANDUM 12-2-58L)

(Title, Unclassified)

The missiles were flight tested and were disturbed in flight by six pulse rockets over a Reynolds number range of 2×10^6 to 21×10^6. These free-flight missiles experienced little induced roll. Extending the body and fins of the shorter missile six diameters changed the fin aspect ratio from approximately 0.04 to approximately 0.02 and increased the value of the lift-curve slope, the dynamic stability, and the drag.

Copies obtainable from NASA, Washington

[redacted]

1. Missiles - Components in Combination (1.7.2.1)
2. Stability, Static (1.8.1.1)
3. Stability, Dynamic (1.8.1.2)
4. Mass and Gyroscopic Problems (1.8.6)

I. Henning, Allen B.
II. NASA MEMO 12-2-58L

NASA

[redacted]